

ABSTRACT

Title of Thesis: PREDICTING WIND PRESSURE ON LOW-RISE BUILDINGS WITH PROTECTIVE PARAPETS USING ARTIFICIAL NEURAL NETWORKS

Yanan Wang, Master of Science, 2020

Thesis Directed By: Associate Professor, Brian M. Phillips,
Department of Civil & Environmental
Engineering

Wind hazards cause tremendous destruction and threaten people's safety and economical losses. To improve current provision toward wind load and strengthen buildings against wind forces, it's vital to properly characterize wind loading on buildings in wind hazard. The turbulence created by the bluff body makes analytical modeling difficult. Therefore, engineers typically turn to wind tunnel tests. This thesis investigates the application of Artificial Neural Networks (ANN) to predict the wind pressure on low-rise buildings with protective parapets. With existing experimental datasets conducted in BLWT, ANN models were trained to model non-linear relationship between inputs, such as tap coordinates and parapet height, and outputs, such as pressure coefficients. The developed model was used to predict pressure coefficients with unseen parapet height to cut down experimental cost.

PREDICTING WIND PRESSURE ON LOW-RISE BUILDINGS WITH
PROTECTIVE PARAPETS USING ARTIFICIAL NEURAL NETWORKS

by

Yanan Wang

Thesis submitted to the Faculty of the Graduate School of the
University of Maryland, College Park, in partial fulfillment
of the requirements for the degree of
Master of Science
2020

Advisory Committee:
Professor Brian M. Phillips, Chair
Professor Chung C. Fu
Professor Amde M. Amde

© Copyright by
Yanan Wang
2020

Dedication

First and foremost, I would like to express my heartfelt gratitude to my thesis advisor, Professor Brian M. Phillips, who gave countless hours to make this thesis a reality. I am indebted for his constant guidance and the tremendous support and opportunities he provided throughout my academic research at University of Maryland.

I would like to thank the effort of my committee member, Professor Chung C. Fu, and Professor Amde M. Amde. They have provided excellent feedback on this thesis, and I appreciate their support and guidance.

I would like to thank my family for their support and encouragement. I would like to thank my mother, Jing Li, for always being there when I need her. She has always been my source of inspiration and she gave me strength to move forward when I thought of giving up.

Acknowledgements

I would like to thank Pedro Luis Fernández Cabán and Michael Lee Whiteman II for providing countless technical guidance and support. Their help has been very valuable throughout my entire research.

The experiment material is based upon work supported by the National Science Foundation under Grant No. 1636039.

Table of Contents

Dedication	ii
Acknowledgements	iii
Table of Contents	iv
List of Tables	vi
List of Figures	vii
Chapter 1: Introduction	1
1.1 Objectives and Motivation	3
1.2 Overview of Thesis	3
Chapter 2: Literature Review	5
2.1 Wind Tunnel History	5
2.2 Pressure Distribution on Low-rise Building	7
2.3 Parapet Effect on Low-rise Building	11
2.4 ASCE Approach for Pressure on a parapet-protected rooftop (Components & Cladding Loads).....	13
2.5 Introduction to Neural Network.....	19
2.5.1 Backgrounds	19
2.5.2 History of ANN' application in Wind engineering.....	22
2.5.3 Impact of Datasets on Performance	23
2.5.4 Impact of Model Complexity on Performance	25
2.5.5 Overfitting and Validation	27
2.5.6 Logistic Regression.....	28
2.5.7 Error Measures and Gradient Descent	29
2.5.8 Initializing and Termination Criteria	31
Chapter 3: BLWT Experiment Setup.....	32
3.1 Facility Setup	32
3.1.1 Introduction of BLWT Facility	32
3.1.2 Terrain Simulation	34
3.2 Building Model Setup	36
3.2.1 Selection of Model Scale	36
3.2.1 Model Geometry	37
3.3 Result Processing.....	39
3.3.1 Data Resource	39
3.3.2 Tap Distribution	39
3.4.2 Pressure Coefficient	41
Chapter 4: Experiment Results and Discussion	43
4.1 Experimental Result Validation.....	43
4.1.1 Pressure Distribution on Rooftop without Parapet	43
4.1.2 Pressure Distribution on Rooftop with Parapet	44
4.1.3 Mitigation Effect of Parapet on Rooftop	48
4.2 Experimental Result Validation by Comparison with ASCE	50
4.2.1 Conversion of Pressure Coefficient C_p	50
4.2.2 Discrepancy between Equivalent GC_p and GC_p from ASCE7-16	55

4.2.3 Discussion on Identified Discrepancy	57
4.3 Sheltering Effect of Parapet on the Rooftop	59
4.3.1 Sheltering Effect at 0° wind (along the short dimension).....	59
4.3.2 Sheltering Effect at 90° wind	63
4.3.3 Discussion on Mitigation Effect of Parapet	67
Chapter 5: Artificial Neural Network Setup	69
5.1 Data Division	69
5.2 Network Architecture and Selection of Parameters	70
5.3 BP Algorithm Selection	72
5.4 Termination Constraint	73
5.5 Chapter Conclusion	74
Chapter 6: Neural Network Results and Discussions	75
6.1 Performance Evaluation of ANN Model	75
6.1.1 Performance Evaluation by Linear Regression.....	75
6.1.2 Performance Evaluation by Learning Curve.....	80
6.1.3 Performance Evaluation by Pressure Distribution	82
6.2 Application of ANN Model	89
6.3 Chapter Summary	91
Chapter 7: Conclusions and Recommendations	92
7.1 Conclusions	92
7.2 Future Studies	93
Bibliography	94

List of Tables

Table 3.1 Details of Measurement configurations and data acquisition	40
Table 5.1 ANN Model Characteristics.....	70
Table 5.2 Types of Backpropagation Algorithm.	72
Table 6.1 Test Error for ANN models.	76

List of Figures

Fig 2.2.1 Wind Flow Regimes on the surface of a low-rise building in 3D.	8
Fig 2.2.2 Wind Flow Regimes on the surface of a low-rise building in 2D.	8
Fig 2.2.3 Conical vortices generated on the windward corner of a low-rise building.10	
Fig 2.2.4 Typical Pressure Distribution on the rooftop of the low-rise building with a range of heights.....	10
Fig 2.4.1 External Pressure Coefficients for Enclosed Building-Wall	15
Fig 2.4.2 External Pressure Coefficients for Enclosed Building-Gable Roof	16
Fig 2.4.3 Diagram for Roof Zones regarding wind loads on components and cladding.	17
Fig 2.4.4 Wind Loads on Parapet.....	18
Fig 2.5.1 Architecture of a Feedforward Neural Network Comprised of 2 Hidden Layers.....	20
Fig 2.5.2 Learning Curves of Different Complexity of ANN Models.....	24
Fig 2.5.3 Target Function of 2 Example Models	25
Fig 2.8.2 Relationship between Network Errors and Model Complexity.....	26
Fig 3.1 Auto-controlled Terraformer's Configuration (Wide Edge; 20mm).....	33
Fig 3.2.1 Isometric view of Building Model (Left).	37
Fig 3.2.2 Front View of Building Model inside BLWT.	38
Fig 3.1.1 Tap distribution on surface panels of the building model.	40
Fig 4.1.1 The distribution of C_p, Min on roof of building model with 0" parapet	44
Fig 4.1.2 The distribution of C_p, Min on roof of building model with 1" parapet	45
Fig 4.1.3 Distribution of C_p, Min on roof of building model with 2" parapet	45
Fig 4.1.4 Distribution of C_p, Min on roof of building model with 3" parapet	46
Fig 4.1.5 Distribution of C_p, Min on roof of building model with 4" parapet	46
Fig 4.1.6 Distribution of C_p, Min on roof of building model with 5" parapet	47
Fig 4.1.7 Location of Selected Tap 132, 168 and 292	49
Fig 4.1.8 Parapet' effect on Minimum Pressure Coefficient of roof taps.....	49
Fig 4.2.1. Durst curve.	52
Fig 4.2.2 Mean Wind Velocity Profile obtained from Cobra Probe Measurements... 53	
Fig 4.2.3 Envelop of pressure coefficients through ASCE7-16 on low-rise building 54	
Fig 4.2.4 Envelope of Equivalent GC_p on roof by Voronoi Diagram	56
Fig 4.3.1 Pressure distribution contour from experiment result at 0" parapet and 0° wind angle.....	60
Fig 4.3.2 Pressure distribution contour from experiment result at 1" parapet and 0° wind angle.	60
Fig 4.3.3 Pressure distribution contour from experiment result at 2" parapet and 0° wind angle.....	61
Fig 4.3.4 Pressure distribution contour from experiment result at 3" parapet and 0° wind angle.....	61
Fig 4.3.5 Pressure distribution contour from experiment result at 4" parapet and 0° wind angle.....	62
Fig 4.3.6 Pressure distribution contour from experiment result at 5" parapet and 0° wind angle.....	62

Fig 4.3.7 Pressure distribution contour from experiment result at 0" parapet and 90° wind angle.....	63
Fig 4.3.8 Pressure distribution contour from experiment result at 1" parapet and 90° wind angle.....	64
Fig 4.3.9 Pressure distribution contour from experiment result at 2" parapet and 90° wind angle.....	64
Fig 4.3.10 Pressure distribution contour from experiment result at 3" parapet and 90° wind angle.....	65
Fig 4.3.11 Pressure distribution contour from experiment result at 4" parapet and 90° wind angle.....	65
Fig 4.3.12 Pressure distribution contour from experiment result at 5" parapet and 90° wind angle.....	66
Fig 4.3.13 Curvature of Shear Layers on Building Models with (Right) and without (Left) Parapets.....	68
Fig 6.1.1 linear regression plots for training, validation and testing subsets of ANN model for the roof.	77
Fig 6.1.2 linear regression plots for training, validation and testing subsets of ANN model for parapets.....	78
Fig 6.1.3 linear regression plots for training, validation and testing subsets of ANN model for walls.	79
Fig 6.1.4 Learning Curves for ANN model developed with Roof data subsets.	80
Fig 6.1.5 Learning Curves for ANN model developed with Wall data subsets.....	81
Fig 6.1.6 Learning Curves for ANN model developed with Parapet data subsets.	81
Fig 6.1.7 Pressure distribution contour of C_p, Min from experiment result (Left) and ANN prediction (Right) at 0" parapet and 45° wind angle.....	82
Fig 6.1.8 Pressure distribution contour of C_p, Min from experiment result (Left) and ANN prediction (Right) at 1" parapet and 45° wind angle.....	83
Fig 6.1.9 Pressure distribution contour of C_p, Min from experiment result (Left) and ANN prediction (Right) at 2" parapet and 45° wind angle.....	83
Fig 6.1.10 Pressure distribution contour of C_p, Min from experiment result (Left) and ANN prediction (Right) at 3" parapet and 45° wind angle.....	84
Fig 6.1.11 Pressure distribution contour of C_p, Min from experiment result (Left) and ANN prediction (Right) at 4" parapet and 45° wind angle.....	84
Fig 6.1.12 Pressure distribution contour of C_p, Min from experiment result (Left) and ANN prediction (Right) at 5" parapet and 45° wind angle.....	85
Fig 6.1.13 Pressure distribution contour of C_p, Max from experiment result (Left) and ANN prediction (Right) at 0" parapet and 285° wind angle.....	85
Fig 6.1.14 Pressure distribution contour of C_p, Max from experiment result (Left) and ANN prediction (Right) at 1" parapet and 285° wind angle.....	86
Fig 6.1.15 Pressure distribution contour of C_p, Max from experiment result (Left) and ANN prediction (Right) at 2" parapet and 285° wind angle.....	86
Fig 6.1.16 Pressure distribution contour of C_p, Max from experiment result (Left) and ANN prediction (Right) at 3" parapet and 285° wind angle.....	87
Fig 6.1.17 Pressure distribution contour of C_p, Max from experiment result (Left) and ANN prediction (Right) at 4" parapet and 285° wind angle.....	87

Fig 6.1.18 Pressure distribution contour of $C_{p, Max}$ from experiment result (Left) and ANN prediction (Right) at 5'' parapet and 285° wind angle.....	88
Fig 6.2.1 Relationship between $C_{p, Min}$ and $C_{p, Max}$ at Various Parapet Height	89

Chapter 1: Introduction

Wind hazards cause tremendous destruction and threaten people's safety and economical losses. Because wind hazard occurs more frequently in smaller magnitude, it is often the dominant lateral load for structural design, in particular for low seismic zones.

For wind hazards like tornados, thunderstorms, and tropical cyclones, the wind is highly turbulent and gusty due to the frictional interaction between the wind and the ground (Holmes, 2001). Generated by the frictional forces and the sharp corners where windward walls meet the roof, vortices are created along the windward edges of the roof. These vortices cause both strong uplifting forces which can damage roof components, and forces into the surface, which are additive to gravity loads. Architectural features such as parapets can mitigate the wind loading on the rooftop by shifting the vortices away from the roof surface.

Because of the turbulence created by bluff bodies such as low-rise buildings, wind loading is difficult to model computationally or analytically. Therefore, engineers turn to wind tunnel tests, which is the primary source for the wind load provisions in ASCE7 (ASCE, 2016). Boundary layer wind tunnel (BLWT) testing is a common aerodynamic experiment method used to simulate the near-surface wind flow with the desired scaled velocity profile and turbulence. Inside a BLWT, air is forced through a tunnel using a set of fans, typically upwind of the tunnel. The floor is equipped with a fetch of barriers that exert drag force and retard wind speed near the ground. The fetch of barriers is called the surface roughness, and it creates height-

varying wind speed and turbulence profile. The retardation effect of surface roughness decreases as height above the tunnel floor increases, eventually disappearing at the gradient height. The boundary layer with the target wind profile is created below the gradient height. To understand the behavior of a parapet-protected building in an extreme weather event, a scaled building model will be tested in BLWT by simulated natural hazard events.

The experiments were conducted at the Natural Hazard Engineering Research Infrastructure of the University of Florida. The building model was instrumented with taps which measures the pressure at a certain location during the test section. Measurements for each instrumented tap were normalized into pressure coefficients C_p . Based on normalized C_p the wind loading on the full-scaled building model was determined. Because the BLWT tests are time-consuming and expensive to conduct, researchers are seeking alternatives such as machine learning to help expand existing experimental datasets. One of the most common models used in machine learning is the artificial neural network (ANN) which uncovers the underlying pattern of overserved data. The network models have superior computation speed and is mostly used to fit nonlinear data points. It's perfect in the case where many experiments have been conducted and there are enough training data.

1.1 Objectives and Motivation

The objectives of this study are to: (1) thoroughly analyze an existing dataset of wind pressure coefficients for a low-rise building with a parapet wall, (2) verify the adequacy of ASCE7 in predicting wind pressure coefficients for buildings with parapets, and (3) develop and apply ANN models that accurately predict/extend wind pressure coefficients to expand previously collected datasets.

1.2 Overview of Thesis

The thesis is organized into seven chapters that describe the approach and findings of this thesis.

Chapter 2 contains mainly two large segments including aerodynamics related topics and ANN related topics. The first part includes the introduction to basic aerodynamic terms and existing knowledge about the wind flow over the flat-roofed low-rise building. It also contains parapets' effect on pressure distribution on low-rise buildings. The chapter also provides the approach for solving pressure on components and cladding (C&N) adapted by ASCE 7-16. The second part of the chapter introduces the basic concepts used in the development of ANN models. ANN network structures and the working mechanism behind-the-scene were introduced. Algorithms and evaluation approach of network performance were discussed in the chapter.

Chapter 3 introduces the setup of the experiment inside of the wind tunnel and the composition of experimental datasets. The chapter presented and validated the configuration of Terraformer for proper terrain simulation. The building model was

also discussed including model scale selection, geometry, and tap distribution. It also discussed the approach to solve for pressure coefficients.

Chapter 4 presented the discussion on experimental results. The pressure distribution of the building model was validated by existing knowledge and the wind -load provision from ASCE7-16.

Chapter 5 focused on the development and validation of developed ANN models. The data division, network architecture and selected algorithms were described in detail along with termination criteria for model training.

Chapter 6 provided validation of network models and demonstrated the performance of the network to predict coefficients accurately. The performance was demonstrated through learning curves and linear regression between true value and prediction. The chapter also discussed the options of optimum parapet height to control the peak suction load on the rooftop.

Chapter 7 summarize the research findings and presented the potential for further studies.

Chapter 2: Literature Review

2.1 Wind Tunnel History

Boundary layer wind tunnels (BLWTs) have been a major tool of simulating wind characteristics in wind engineering and related disciplines for years. Because of the turbulent nature of wind flow around bluff bodies, the pressure acting on structures fluctuates greatly. These fluctuations make predicting wind loading on buildings difficult. In structural engineering, the BLWT test has been used for decades to help characterize wind loading and develop wind loading provisions.

Before BLWT became widespread, the best practice of coding officials to determine the wind loading was through a ‘quasi-steady’ assumption. This method allows peak pressures to be calculated as the product of mean pressure coefficient and gust wind speed. Peak pressure produced by this method tend to be conservative for large wind areas. Also, it is not possible to account for the effect of fluctuations. Later, researchers started to conduct aerodynamic tests in the wind tunnel with uniform wind flow. However, pressure variation in shear layers of uniform flow was remarkable and induced a lot of error. It was not until 1932 a German researcher, Flachsbarth, observed the relatively stable characteristics of boundary layer flow and started to study wind effect on the building. In 1965, Jensen revisited Flachsbarth’s observation and constructed a small wind tunnel to generate boundary layers with fans and roughness elements on the floor inside the tunnel. He proposed Jensen’s number, a ratio of building height to roughness length, and concluded it as an important parameter for modeling natural wind.

In the 1970s there were two typical boundary layer wind tunnels used. One type of tunnel was the closed-circuit design and the other type of tunnel was an open circuit with a fan installed downstream. As technology advanced, the most used BLWT today is open circuit type with fans upstream blowing air through the tunnel (Holmes, 2001).

2.2 Pressure Distribution on Low-rise Building

Wind flow impacts building surfaces, generating pressure either positive (acting towards the surface) or negative (acting away from the surface). The direction and magnitude of pressure fluctuate due to the turbulent nature of approaching wind and unsteady flow generated by the bluff body surfaces. The three main sources of pressure fluctuation include 1) natural turbulence in freestream flow 2) unsteady flow generated by building surface 3) fluctuating forces due to building's motion. Since the boundary layer simulated is relatively stable and the building model (in this study) is not aeroelastic, the effect of natural turbulence and movement of the building can be neglected in terms of turbulence magnitude. Natural turbulence in freestream and unsteady flow generated by wind impacting with the building surface are the two sources of turbulence.

For a low-rise building with a surface normal to wind direction, the flow around the building follows the pattern indicated in Fig 2.2.1. As wind approaches the building, the flow gets separated from the bluff body contour at leading-edge corners. The separated region near the bluff body is defined as a free shear layer which is a thin layer of flow that has high shear and vorticity. These unstable thin shear layers would roll up forming vortices. As vortices travel along model surfaces it will create a strong suction force on its 'footprint'. The vortices are the major reason for pressure fluctuation. If the bluff body is long enough for the development of reattachment, vortices would roll along the surfaces and causing pressure variation as it travels.

The pressure acting on the interior region of the windward wall is positive, and pressure decreases to zero and even becomes negative near separation zones

along three edges. Pressure distribution on sidewalls have a generally similar pattern with higher suction along the roof edge and the magnitude drops as height decreases. After separated shear layer reattached to building contour along wind direction, the turbulent shear layers would circulate along the leeward walls creating negative pressures.

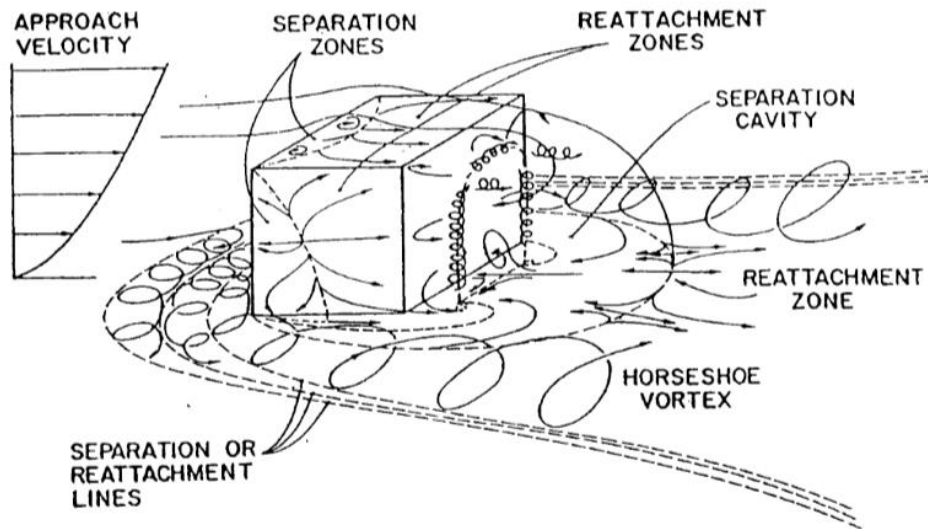


Fig 2.2.1 Wind Flow Regimes on the surface of a low-rise building in 3D.
Adapted from 'Roof Uplift Mechanisms' (Peterka, 1989)

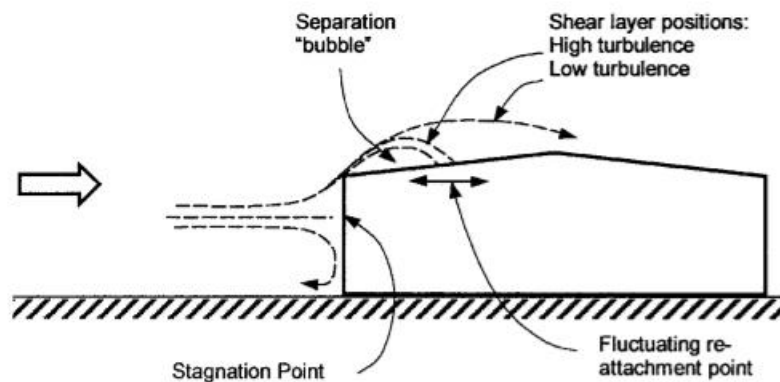


Fig 2.2.2 Wind Flow Regimes on the surface of a low-rise building in 2D.
Adapted from 'Wind Loading of Structures' (Holmes, 2001)

When the wind direction is oblique to the building surfaces, different types of vortices are created shown in Fig 2.2.3, conical vortices, which are like those found on delta-wings of aircraft (Holmes, 2001). Suction loads under these vortices are the largest over low rise building with a low-sloped roof. Past studies on low rise building situated in an open terrain had suggested that roof corner suction would reach peak level at quartering wind (45°). On the roof where separation and reattachment both occur, pressure magnitude and direction vary greatly. Based on extensive study results, the pattern of roof pressures distribution is comprised of a heavily loaded up-wind corner and edges which in compacts with oblique wind and a lightly loaded interior area as shown in Fig 2.2.4. ASCE7-16 has adopted a scheme of pressure distribution on the roof based on Kopp's research. It consists of four 'L-shaped' corner zones, four edges, and two coincided interior rectangular zones with different pressure magnitude (Kopp et al., 2015^a). The details regarding distribution on the roof will be discussed in Chapter 2.4. It's of critical importance to design strong components and cladding for the corner and edges zones to resist uplift forces.

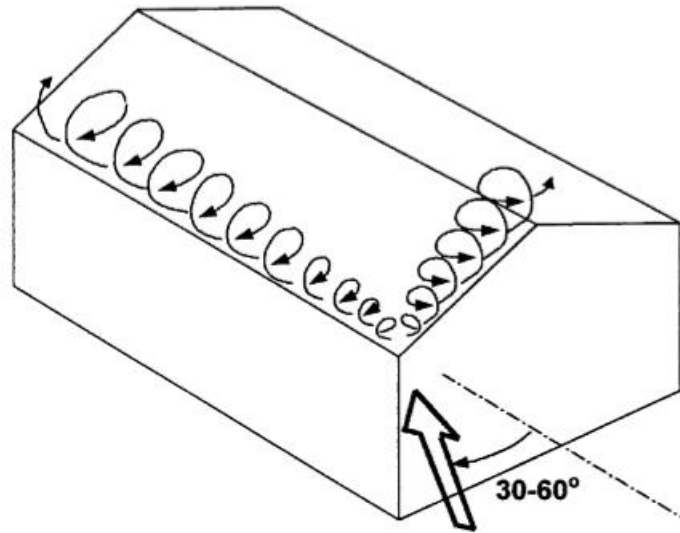


Fig 2.2.3 Conical vortices generated on the windward corner of a low-rise building.
Adapted from 'Wind Loading of Structures' (Holmes, 2001)

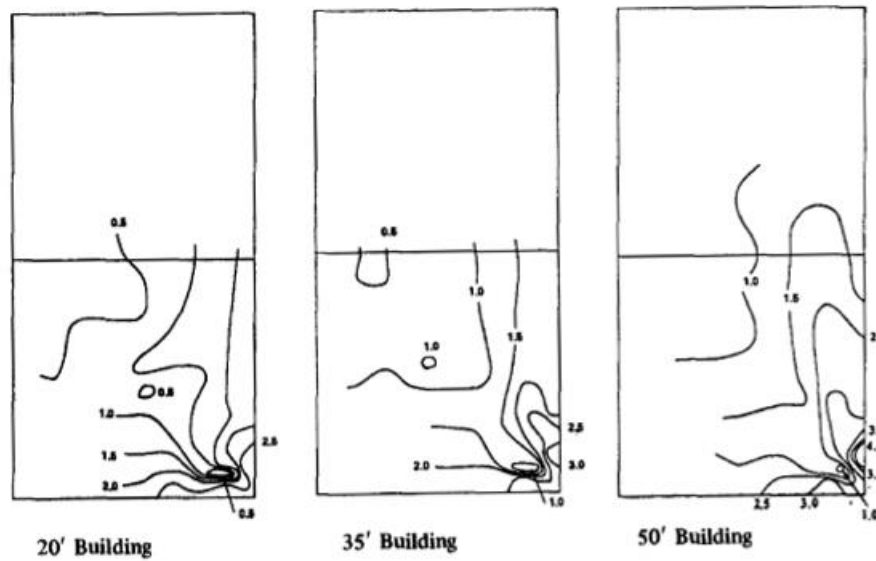


Fig 2.2.4 Typical Pressure Distribution on the rooftop of the low-rise building with a range of heights.
Adapted from '*WIND LOADING OF FLAT ROOFS WITH AND WITHOUT PARAPETS*' (Lythe and Surr, 1983)

2.3 Parapet Effect on Low-rise Building

Since wind loading on the roof is essential to the design, the architectural details locating on the roof is of the same importance. As discussed in the previous section, separating shear layers and vortex shedding results in pressure fluctuation on a bluff body and conical vortices generates the highest suction on the up-wind corner. To mitigate local extreme pressure, the conical vortices must be interrupted and guided away from the roof surface by the parapet wall.

Many types of research have examined the effect of the parapet on wind pressure distribution. It is generally recognized parapets could reduce the worst suction load by shifting vortex reattachment. However, experiments show that it's not always helpful to have a parapet because a short parapet may increase the worst pressure on the roof (Stathopoulos, 1981; Kopp et al., 2005^a; Huang et al., 2017). Stathopoulos concluded for parapet with relative height (h/H) between 0.125 and 0.25, the maximum local suction could be reduced up to 30% and the interior positive pressure could be increased by around 5% (Stathopoulos, 1981). Kopp concluded solid perimetric parapets with $h/H > 0.25$ generally reduces the mean and peak pressure by up to 50% in the corner region (Kopp et al., 2005^a). He also mentioned conical vortices were detached from the roof surface in the corner region and the pressure distribution was nearly uniform with magnitude significantly reduced (Kopp et al., 2005^a). Many researchers have conducted their test on a relatively small building model scale (1:50, 1:100) but not a lot on large scales. In 2017 a test was conducted to validate the mitigation effect of solid on a large-scale model. The building scale was 1:20 and the height to width ratio was 1:1. It's concluded

reduction effect grows rapidly when h/H ranges between 0.01 and 0.15. The mitigation effect of the parapet was inhibited at $h/H > 0.15$. The result agreed with previous studies concluded that mean pressure variation became milder as height increased and the mitigation of extreme pressure was inhibited with a relative height greater than 0.15 (Huang et al., 2017).

Based on the available literature, tall ($h/H > 0.1$) solid perimetric parapet does help mitigating peak suction load in corner and edge regions. Short parapets can worsen the situation. It's of critical importance for structural designers to understand wind loads on building surfaces to perform safe design.

2.4 ASCE Approach for Pressure on a parapet-protected rooftop (Components & Cladding Loads)

ASCE 7-16 Chapter 30 applies the directional procedure and envelope procedure to solve for design pressures with specific equations applicable to each component and cladding (C&C) surface. The external pressure coefficient factor (GC_p) provided in ASCE diagrams were developed based on wind tunnel testing measurements of prototype building conducted at the University of Western Ontario. (Kopp and Morrison, 2014). The tests were conducted for two roughness categories, B and C, simulating upwind terrain of urban and suburban to open and flat conditions. Factors that affect GC_p include the specific location on the building, the height above the ground, the relative location to boundaries (i.e. rooftop zones), and the geometry of the building. Because the approach wind direction is not known, factors are enveloped over all wind directions. The results were also normalized for directionality and exposure effects. Therefore, the value GC_p represents the upper bounds of the most severe values for any wind direction (ASCE7-16)

Out of the six-part in chapter 30, the first part is applicable for a low-rise building ($h < 60ft$) with a low slope roof. The design wind pressure is determined through equation as followed,

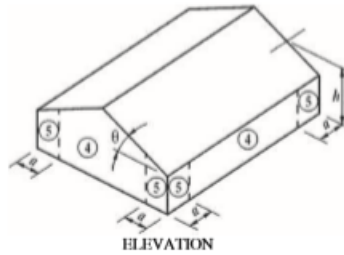
$$p = q_h[(GC_p) - (GC_{pi})]$$

Where q_h is the velocity pressure evaluated at mean roof height h ; GC_p represents the external pressure coefficients given in diagrams based on different roof type; GC_{pi} is the internal pressure coefficient. q_h is determined through the combination of basic wind speed and types of wind load parameters (i.e. $K_d, K_{zt}, K_e, K_d, etc.$). The wind

pressure on different types of C&C are corrected by GC_p factors from applicable diagrams. The GC_p factors are given for walls and types of roofs. Many diagrams were referred to in part 1 and 6 corresponds to the flat-roofed low-rise building. In Fig 2.4.1, the positive and negative wind pressure coefficients are determined by the effective wind area of the component located on sidewalls (Corner and Edges).

The negative roof pressure diagram shown in Fig 2.4.2 was modified based on new findings of Kopp and Morrison (2016) who examined the effect of building height on spatial patterns and magnitudes of area-averaged pressure coefficients. They found the current edge zone size $a = 0.4h$ in ASCE7-10 could not be made to work concerning interior zone pressure coefficients (Kopp and Morrison, 2016). Modifications were made to create a new pattern that has L-shaped corners (zone 3) with a width of $0.2h$ from the edge of the roof and length of $0.6h$ along both edges. In Fig 2.4.2, the positive and negative wind pressure coefficients are determined by the effective wind area of the component located on the rooftop. Based on the size of the rooftop, there're 4 scenarios of roof zones on low-rise buildings shown in the Fig 2.4.3. For the building model used in this research, both zone 2 and 3 exist along the long edge while only zone 3 exists along the short edge. The spatial pattern of pressure on the roof belongs to category (d). According to the effective wind area of $1ft^2$, $GC_p = -2.3$ for Zone 2 and $GC_p = -3.2$ for zone 3.

Diagram



Notation

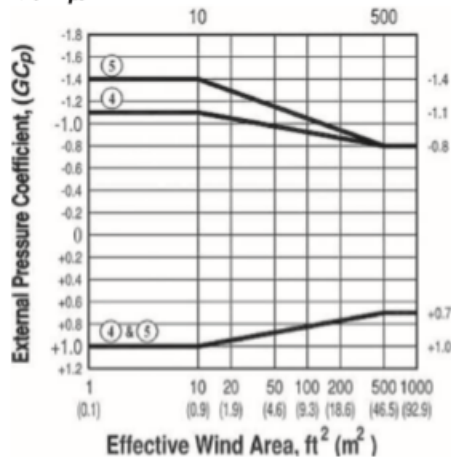
a = 10% of least horizontal dimension or $0.4h$, whichever is smaller, but not less than either 4% of least horizontal dimension or 3 ft (0.9 m).

Exception: For buildings with $\theta = 0^\circ$ to 7° and a least horizontal dimension greater than 300 ft (90 m), dimension a shall be limited to a maximum of $0.8h$.

h = Mean roof height, in ft (m), except that eave height shall be used for $\theta \leq 10^\circ$.

θ = Angle of plane of roof from horizontal, in degrees.

External Pressure Coefficient, (GC_p) - Walls



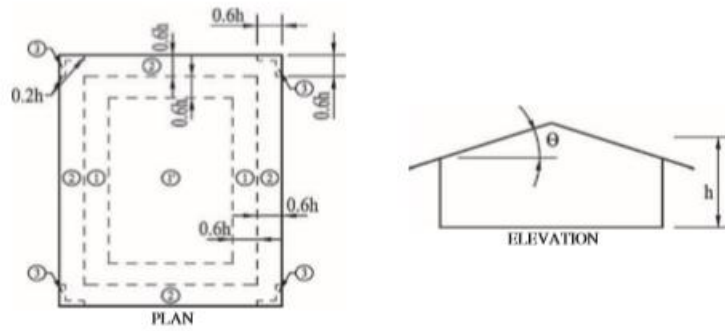
Notes

1. Vertical scale denotes (GC_p) to be used with qh .
2. Horizontal scale denotes effective wind area, in ft² (m²).
3. Plus and minus signs signify pressures acting toward and away from the surfaces, respectively.
4. Each component shall be designed for maximum positive and negative pressures.
5. Values of (GC_p) for walls shall be reduced by 10% when $\theta \leq 10^\circ$.

FIGURE 30.3-1 Components and Cladding [$h \leq 60$ ft ($h \leq 18.3$ m)]: External Pressure Coefficients, (GC_p), for Enclosed and Partially Enclosed Buildings—Walls

Fig 2.4.1 External Pressure Coefficients for Enclosed Building-Wall
Adapted from 'Minimum Design Loads for Buildings and other Structures', (ASCE, 2016)

Diagrams



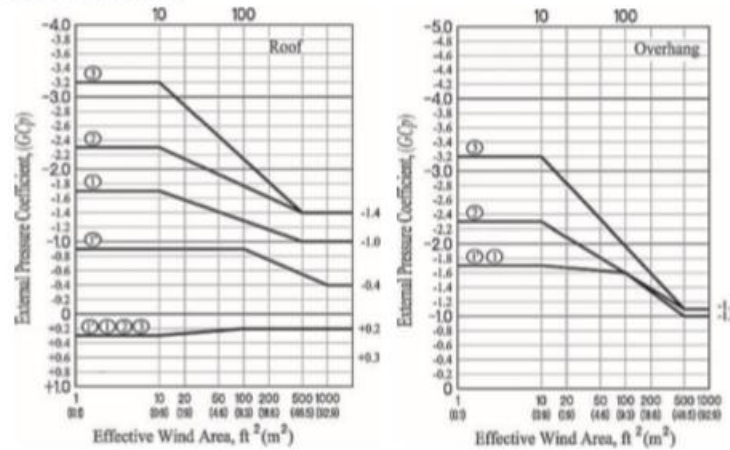
Notation

B = Horizontal dimension of building measured normal to wind direction, in ft (m).

h = Eave height shall be used for $\theta = 10^\circ$.

θ = Angle of plane of roof from horizontal, in degrees.

External Pressure Coefficients



Notes

1. Vertical scale denotes (GCP) to be used with q_h .
2. Horizontal scale denotes effective wind area, in ft² (m²).
3. Plus and minus signs signify pressures acting toward and away from the surfaces, respectively.
4. Each component shall be designed for maximum positive and negative pressures.
5. If a parapet equal to or higher than 3 ft (0.9 m) is provided around the perimeter of the roof with $\theta \leq 7^\circ$, the negative values of (GCP) in Zone 3 shall be equal to those for Zone 2, and positive values of (GCP) in Zones 2 and 3 shall be set equal to those for wall Zones 4 and 5, respectively, in Fig. 30.3-1.
6. Values of (GCP) for roof overhangs include pressure contributions from both upper and lower surfaces.
7. If overhangs exist, the lesser horizontal dimension of the building shall not include any overhang dimension, but the edge distance, a , shall be measured from the outside edge of the overhang.

FIGURE 30.3-2A Components and Cladding [$h \leq 60$ ft ($h \leq 18.3$ m)]: External Pressure Coefficients, (GCP) , for Enclosed and Partially Enclosed Buildings—Gable Roofs, $\theta \leq 7^\circ$

Fig 2.4.2 External Pressure Coefficients for Enclosed Building-Gable Roof
Adapted from 'Minimum Design Loads for Buildings and other Structures' (ASCE, 2016)

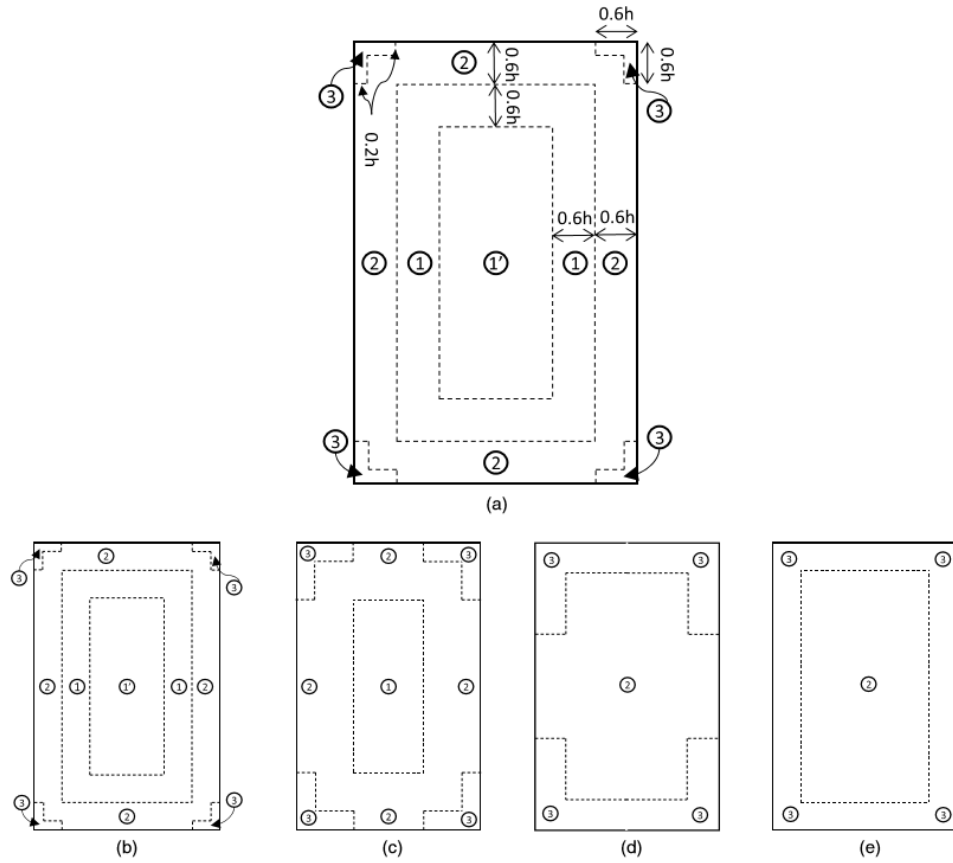


Fig 2.4.3 Diagram for Roof Zones regarding wind loads on components and cladding. Adapted from 'Component and cladding pressures and zones for the roofs of low-rise buildings.' (Kopp and Morrison, 2014)

Chapter 30 also divides a separate section to demonstrate wind loads on building appurtenances such as roof overhangs, parapets, and rooftop equipment. The wind pressure for parapets are represented by p_i in the Fig 2.4.4.

To solve for pressure distribution of parapet, the key is to find the pressure coefficients corresponding to the location of parapets on the rooftop. As noted in Fig 2.4.1, coefficients should be read from Fig 2.4.1 and Fig 2.4.2 which corresponds to pressure coefficients in Pos/Neg wall and roof pressure zone. For interior regions of the parapet, the wind pressure coefficients are the same as the coefficient for adjacent roof regions. For outer regions of the parapet, the wind pressure depends on the coefficients of different zones of the walls.

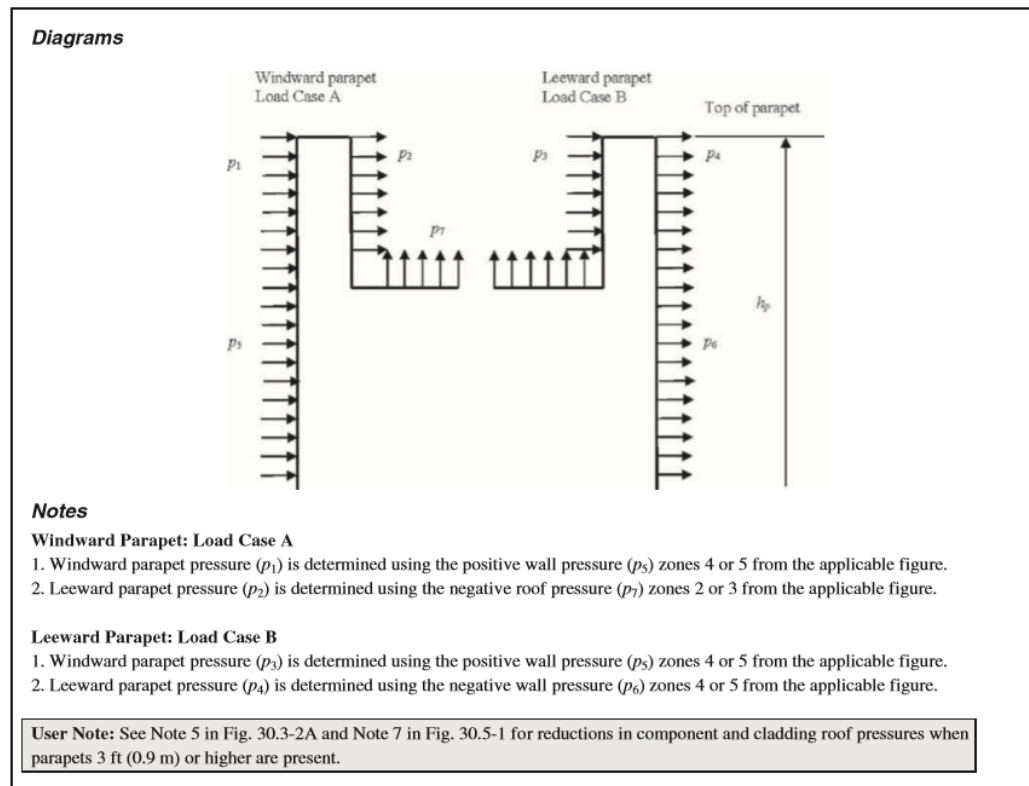


FIGURE 30.8-1 Components and Cladding, Part 6 (All Building Heights): Parapet Wind Loads, All Building Types—Parapet Wind Loads

Fig 2.4.4 Wind Loads on Parapet.

Adapted from 'Minimum Design Loads for Buildings and other Structures'(ASCE, 2016)

2.5 Introduction to Neural Network

2.5.1 Backgrounds

When the analytical solution couldn't be found to describe the pattern of numbers, there's always a way to simply use data to construct an empirical solution (Yaser, 2012). Having the same objective as an analytical solution, an empirical solution seeks an unknown function which depends on unknown variables. The approach to uncover the underlying function of overserved data is machine learning. Having superior computation speed, computer models are developed to learn from data. One of the models commonly utilized to fit nonlinear data points is an artificial neural network (ANN). Same as neural networks inside the brain of intellectual animals, ANN could refine itself through training. There are two types of learning namely supervised and unsupervised. When a network is trained with data input that has corresponding correct output as guidance, it's called supervised learning and vice versa (Barlow, 1989) The widest application of supervised learning is the neural network.

Network is a symbolization of the unknown target function that yields the correct output (Schmidhuber, 2015). The structure is expected to be complex for its ability to unveil patterns that no analytical model could. Fig 2.5.1 is an example of a feed-forward neural network. The individual units that constructed the entire neural network is called a neuron. Arranged in columns, a series of parallel neurons form a layer. Each neuron of a layer is connected to all neurons in the next layer. Thinking the intermediate part as a black box, the network only consists of two layers, the input

layer, and the output layer. Information flows from the input (left) layer to output (right) layer through nodes and links.

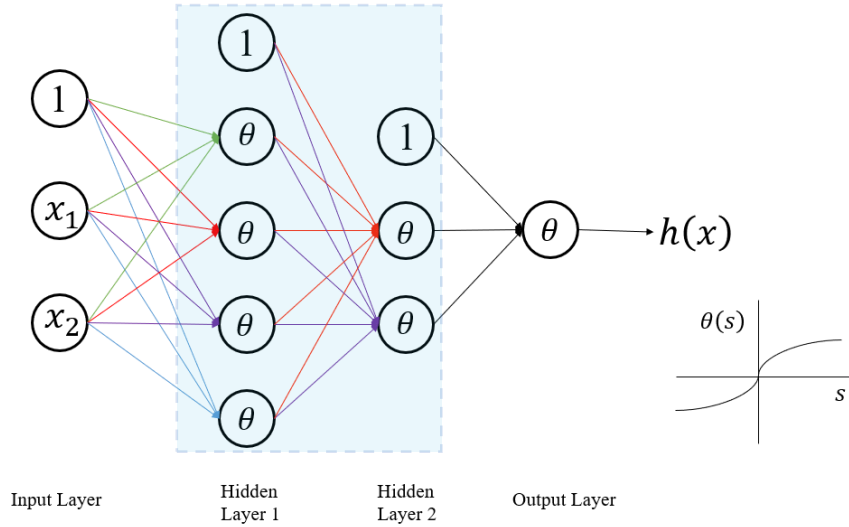


Fig 2.5.1 Architecture of a Feedforward Neural Network Comprised of 2 Hidden Layers.

Node is a portal of receiving numerical data such as x_i and θ_j as input for the next layer (Schmidhuber, 2015). The link connecting two nodes is assigned a weight based on the important contribution of the node. In each layer, a node of 1 is added to account for bias. For each neuron in each layer, the product of weight and node input from the previous layer are summed together. The product $s = 1 * w_{1j} + \sum x_i * w_{ij}$ is then plugged into transfer function $\theta(s)$. The transfer function helps with reducing computation time expense by converting a large number into smaller values, and the range typically varies from -1 to 1 depending on the choice of the transfer function. Then the result of $\theta(s)$ becomes the input to the next following layer. At the far end of the network, $\theta(s)$ is reversibly transferred back into the same order of original input. By comparing the output to a true value, network performance can be evaluated

by percentage difference defined as in-sample-error. To modify weights an algorithm called backpropagation (BP) is introduced. Through the BP algorithm, weights in all layers are changed simultaneously and yield fresh output supposing closer to the true value (Dreyfus, 1962). After the network is done training, a fresh set of data is fed into the network for testing, and the out-of-sample error is expected to be small. One measure of a network's ability to adapt properly to previously unseen data is Generalization (Yaser, 2012). It's achieved when both in-sample-error and out-of-sample error are minimized. It indicates network generalize well for in-sample data as well as out-of-sample data. After training is accomplished, the network should be able to categorize a fresh input based on the recognized pattern.

2.5.2 History of ANN' application in Wind engineering

BLWT testing has been popular for decades in wind engineering for its superior contribution to evaluating wind load. However, the time and financial expenses for conducting such tests remain relatively high. As technology advances, the power of intellectual machine learning should be incorporated into the traditional wind tunnel tests. Many researchers have tried to apply ANN to characterize wind loading on structures. Y. Chen (2002) focused on the prediction of mean and RMS pressure coefficients on gable roofs of low-rise buildings. The prediction accuracy of ANN models for fresh cornering wind angles was demonstrated by an average error of less than 2% (Chen et al., 2002). Facundo (2017) developed three computational models making use of three types of ANN to predict the wind pressure coefficients on surfaces of flat, gable and hip-roofed buildings. The maximum percentage error using FANNs for three types of roof is 2.3%, 3.2% and 4.2% accordingly (Facundo et al., 2017).

2.5.3 Impact of Datasets on Performance

The performance of a network depends on the size of the dataset. Based on the Hoeffding Inequality,

$$P[|v - \mu| > \epsilon] \leq 2e^{-2\epsilon^2 N}$$

Where v is the observation from samples, μ is observation outside samples, ϵ is error tolerance, N is the number of data; $|v - \mu|$ represents the difference between true value (v) and generated output (μ). The inequality equation indicates the probability of making a bad prediction drops as the sample size (N) increases. Therefore, network performance is exponentially unlikely to drop below the threshold as the sample size increase. That's why all available data were used for developing a good network.

As stated previously, larger dataset contributes to better generalization performance.

In the next graph error of two network models is plotted against the number of data points (N). The error curve of a simple model is shown in Fig 2.5.2 to the left. E_{out} and E_{in} start high and gradually leveled out as N increase. A complex model is shown to the right. E_{in} starts at zero and E_{out} is infinity. As more data become available for the development of a complex model, the overall expected error drops gradually and remain at a lower level. It's concluded that a complex model yields a better model with conditions of large datasets.

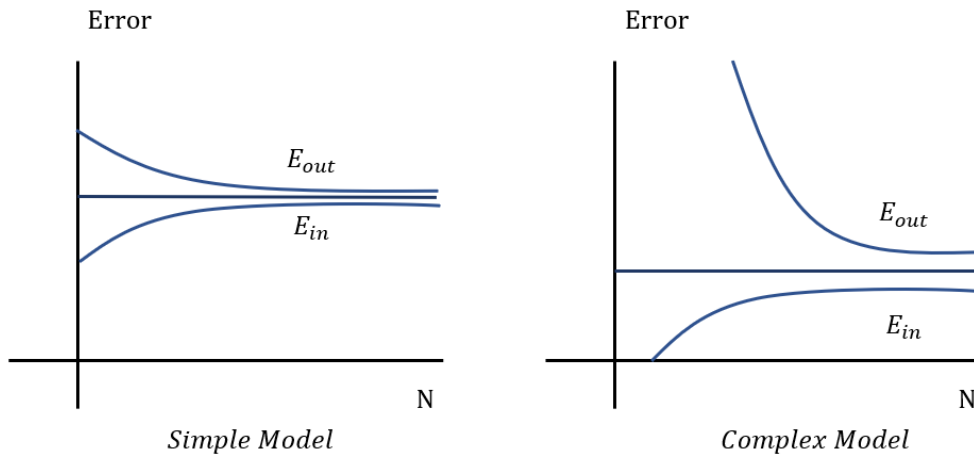


Fig 2.5.2 Learning Curves of Different Complexity of ANN Models

2.5.4 Impact of Model Complexity on Performance

A complex network doesn't always guarantee good performance. The size of a dataset's not the only parameter affecting network performance. Model complexity, in another word the number of effective neurons in each of the hidden layers, plays an important role. See Fig 2.5.3 for illustration. The horizontal variable, VC dimension, denotes the number of effective training parameters that best characterize target function. As model complexity increases, out-of-sample error drops at first until it hits local minima and starts to increase. With an appropriate model complexity, a perfect balance of in-sample and out-of-sample error exists at d_{VC}^* . At this ideal situation network performance could reach maximum with minimum calculation expanses.

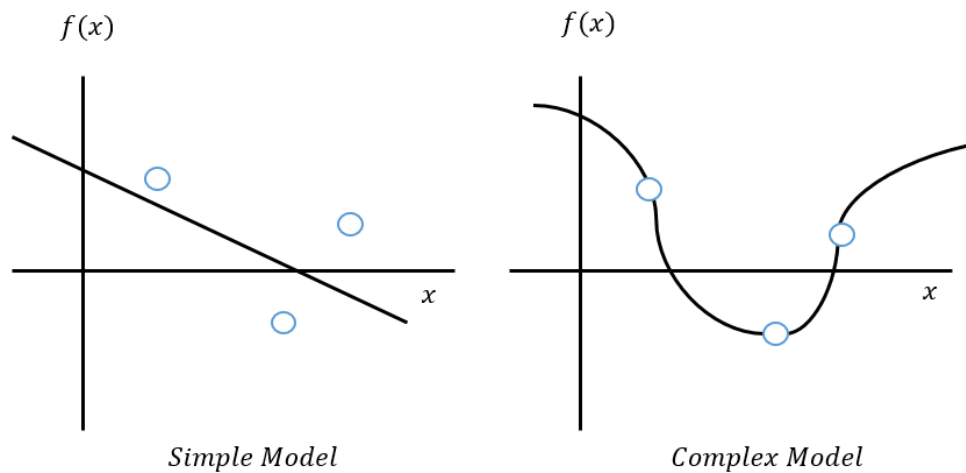


Fig 2.5.3 Target Function of 2 Example Models

Take a linear target function for an example. A simple 1st order linear model (Fig 2.5.3, Left) could fit three data points with moderate gaps between points and fit line. A higher-order complex model (Fig 2.5.3, Right) fits 3 data points with a polynomial function by passing through each one of them. For the given example, the

number of data of $N = 3$ is not compatible with high model complexity. With acknowledge that target function being linear, the complex function would yield high E_{out} even E_{in} is low. It can also be validated by error curves in Fig 2.5.4.

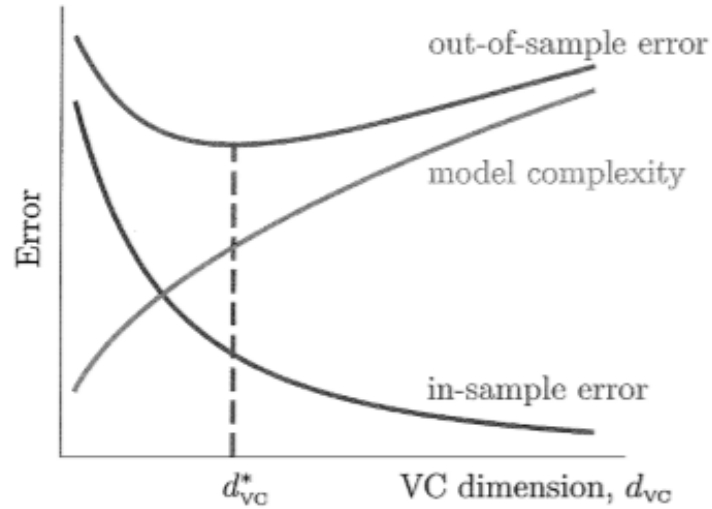


Fig 2.8.2 Relationship between Network Errors and Model Complexity. Adapted from 'Learning from Data' (Yaser, 2012)

2.5.5 Overfitting and Validation

Compared to the simple model, the generalization of the complex model is diminished as a tradeoff of low E_{in} . When a model is more complex than its necessary to represent target function, E_{out} starts to increase and yielding an inferior hypothesis of the target function (Yaser, 2012). The phenomenon is called overfitting which's an indication of the model starts to fit stochastic and deterministic noises in datasets. Overfitting occurs because, in the training process, the network keeps exploring and added an effective parameter d_{VC} to reach a global minimum of E_{in} . Although E_{out} acts like an indicator for the network to stop incorporating extra parameters, E_{out} won't be available until the end of the training. Considering bias to be produced potentially, the test set must be uncontaminated, and testing is not initiated until training is complete. Therefore, the best way is to replace E_{out} with similar error terms, that is obtained from another portion of the dataset. The newly introduced error term E_{val} is obtained along with training through validation.

Validation is achieved by tuning parameters (Weights and bias) of network with a portion of non-train data. The whole dataset is divided up into three portions accordingly for training, validation, and testing. A common division is 70-15-15 which's balanced between relatively large training sets and reasonable amounts of data for tuning and testing. The curve for expected E_{val} can demonstrate the network's performance and be used to identify d_{VC}^* once E_{val} starts to increase.

2.5.6 Logistic Regression

The products of weight and input are combined linearly and defined as signal input S . The value of signal input is unbounded, and it can be taken as output directly for a model with a linear target function (Yaser, 2012). The algorithm used by this model is linear regression. In the case where target function yields bounded output, a logistic function $\theta(s)$ is applied to the signal input, and the output takes the form of probability. The algorithm is logistic regression and it has wide application in practice. The logistic function is usually monotonic increasing and bounded by a range of values. The most commonly used logistic function is sigmoid $\theta(s) = \frac{e^s}{1+e^s}$ whose output is between 0 and 1. Another popular function is hyperbolic tangent $\theta(s) = \frac{e^s - e^{-s}}{e^s + e^{-s}}$ that yields output between -1 and +1.

2.5.7 Error Measures and Gradient Descent

The error measure $e(h(x), y)$ used in logistic regression is based on likelihood. It indicates how likely the output y will be predicted correctly by hypothesis $h(x)$. The pointwise in-sample-error E_{in} is summed together $E_{in}(w) = \frac{1}{N} \sum_{n=1}^N e_n$ given a set of weight w in layer l . To tune, the weight vector gradient descent method was used by taking steps toward a negative gradient direction (Baird, 1999). New weight vector at layer l is calculated as the following equation,

$$w(t + 1) = w(t) - \eta \nabla E_{in}(w)$$

Where t denotes training epoch and w is weight vector at t . ∇E_{in} denotes the gradient of w in layer l . The size of the training step, η , measures how large the step is for w to descent. The most effective gradient descent pattern initiates with relatively large step for speed and gradually become smaller as ∇E_{in} decrease (Schmidhuber, 2015). If E_{in} can be monitored by a hilly surface, the gradient descent algorithm drives $E_{in}(w)$ toward the bottom of a valley (Yaser, 2012). Considering not overshooting the global minimum of E_{in} , it takes a lot of rounds to go downhill with time-varying η that gets smaller as E_{in} gets closer to the bottom.

To compute the gradient, derivative of E_{in} concerning w of layer l must be solved as the followed equation,

$$\nabla E_{in}(w) = \frac{\partial E_{in}}{\partial w^{(l)}} = \frac{1}{N} \sum_{n=1}^N \frac{\partial e_n}{\partial w^{(l)}}$$

There's no closed-form solution for the equation in ANN, and one way to solve is the numerical finite difference approach. It can be extremely time-consuming because the iteration is unceasing until E_{in} reaches the global minimum. A more efficient method

is adopted and defined as Back Propagation (BP) which utilizes a set of chain rules to combat the difficulty of computation (Dreyfus, 1962). The BP algorithm takes a detour for calculation of partial derivative $\frac{\partial e_n}{\partial w^{(l)}}$ by using a combination of sensitivity $\delta^{(l)}$ and input from the previous layer $x^{(l-1)}$. The formula below quantifies how e changes with $s^{(l)}$,

$$\delta^{(l)} = \theta'(s^{(l)}) \times [w^{(l+1)} \delta^{(l+1)}]_1^{d^{(l)}}$$

Where $\delta^{(l)}$ denotes the sensitivity of layer l . $s^{(l)}$ denotes input signal that goes into layer l in forward propagation. θ' is the derivative of transform function in layer l .

For $\theta = \tan^{-1} s$, $\theta'(s^{(l)}) = [1 - x^{(l)} \times x^{(l)}]_1^{d^{(l)}}$. Using the equation above,

sensitivity for each layer can be solved for a single input data point. Then sensitivity for each layer is plug into the formula below for $\frac{\partial e_n}{\partial w^{(l)}}$

$$\frac{\partial e_n}{\partial w^{(l)}} = x^{(l-1)} (\delta^{(l)})^T$$

With sufficient calculation for gradients, the weight vectors are tuned accordingly for every data input. The running time is the order of the number of weights in the network since one forward and one backward propagation is run over a single data input (Schmidhuber, 2015).

2.5.8 Initializing and Termination Criteria

The initial weight vector $w^{(l)}$ was set at small random values such that $\theta(wx)$ is close to zero. The reason is that it allows weight vectors to be tuned flexibly, and the effect of gradient descent is more notable with gradient moving toward either positive or negative direction.

Since the target surface could have multiple local minima, stopping training only depending on the order of gradient can cause premature termination. The best state for termination is when a continuous series of marginal error improvements are found and the number of iterations is bounded by a set max value.

Chapter 3: BLWT Experiment Setup

3.1 Facility Setup

3.1.1 Introduction of BLWT Facility

The experiments were conducted in the Boundary Layer Wind Tunnel (BLWT) at the Natural Hazard Engineering Research Infrastructure of the University of Florida. The tunnel has a dimension of 6.1 m x 6.1 m x 31.75 m. The end of the tunnel is equipped with 8 Aerovent vaneaxial fans that can generate speeds up to 18 m/s. During the test, fans were kept running at 1050 RPM corresponding to a wind speed of 14 m/s.

Shown in Fig 3.1, the BLWT is equipped with the automated continuously adjustable terrain roughness field (the “Terraformer”). The model is mounted on a 1-meter diameter turntable that could rotate 360° along the centerline for desired exposure to wind. Other instrumentation includes a Scanivalve pressure scanning system, which’s mounted under the turntable. The tunnel is also equipped with four turbulent flow instrument cobra probes that measure three components of velocity up to 2000 Hz. The probes are mounted on a transverse gantry to allow for positioning within the tunnel’s cross-section.

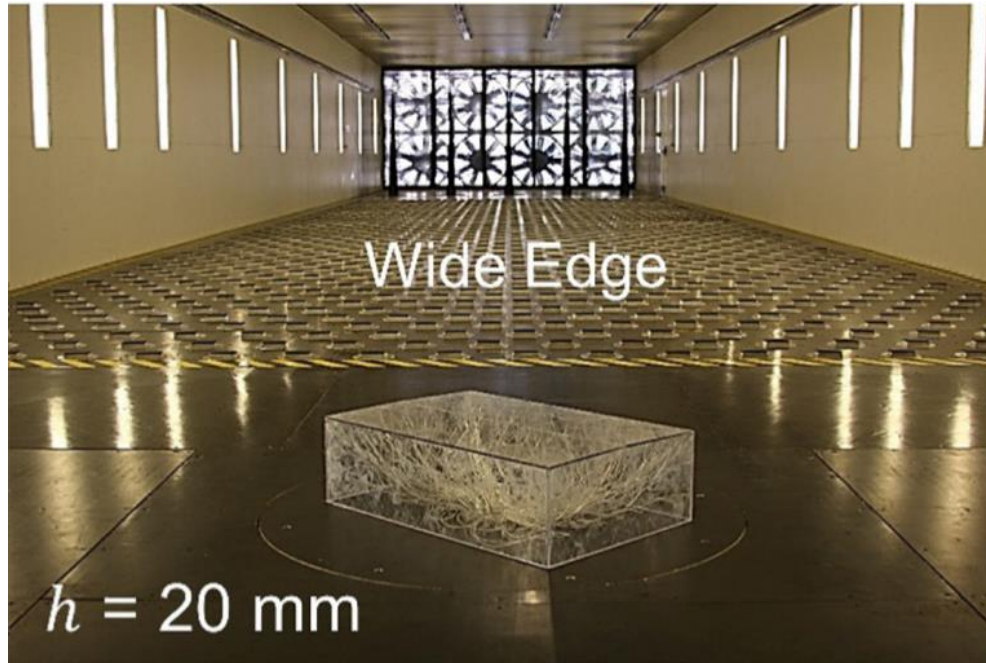


Fig 3.1 Auto-controlled Terraformer's Configuration (Wide Edge; 20mm).
Adapted from 'Predicting Roof Pressures on a Low-Rise Structure From Freestream
Turbulence Using Artificial Neural Networks' (Fernández et al., 2018)

3.1.2 Terrain Simulation

Upwind terrain condition was simulated by Terraformer which's an automated roughness element grid composed of 1116 roughness elements that could rapidly change its orientation and height. The element has a plan dimension of 10 cm by 5 cm. They are spaced 30 cm away from each other in a staggered arrangement. The system is fully automated controlled. They can be raised to 160 mm above ground and be rotated by 360° along the centerline. When the surface of the long dimension impacts wind, the arrangement is called the Wide Edge. Similarly, it's called Short Edge when the short dimension impacts wind. For this study, open terrain was chosen to be modeled as a terrain condition in a full-scale model. The elements were configured to be 20 mm tall with the wide edge windward.

Fang (1994) concluded that extreme pressure correlates with a few parameters including roughness distribution, eave height turbulence intensity, and eave height integral length scale (Fang and Sill, 1994) Roughness length (Z_0) is related to surface roughness characteristics of upper terrain definition. The velocity profile of the boundary layer varies concerning height, and velocity fluctuates near the ground due to shear-generated turbulence. The turbulence length scales (L_x) is a measure of the temporal lag of the fluctuating velocity inflow direction which is represented as a separation distance using Taylor's hypothesis (Emes et al. 2018). To validate generated boundary layer characteristics of open terrain, roughness length and longitudinal integral length were determined for comparison with standard from ASCE7-16. The two parameters, L_x and Z_0 , are calculated with a 1:18 model scale. To solve for roughness length, equations, as followed, were used.

$$u_* = \left(\overline{u'^2} + \overline{v'^2} + \overline{w'^2} \right)^{1/4}$$

$$z_0 = (z - d) e^{\left[\frac{U(Z) * K}{u_*} \right]}$$

Where u_* is shear (friction) velocity calculated from three components of velocity (u, v, w); z_0 is roughness length; z is desired height and $U(Z)$ is mean wind speed at height z ; d is zero-plane displacement height; K is von Karman's constant. Roughness length (z_0) was calculated to be 1.59 mm. It corresponds to 0.03 m of roughness length in the full-scale model and lies within the range of surface roughness for exposure C in ASCE7-16.

Based on longitudinal turbulence spectra, the longitudinal integral length scale (L_x) was 1.06 m at height of 610 mm. It corresponds to L_x of 18 m in the full-scale model at height of 11 m. The result of a longitudinal integral length of 18 m does not meet the standard of 110 m in ASCE/SEI 49-12. The discrepancy of the longitudinal length scale was due to insufficient turbulence simulation in BLWT. For a relatively large model scale like 1:18, a sacrifice of an integral length scale must be made as a tradeoff of pressure resolution.

3.2 Building Model Setup

3.2.1 Selection of Model Scale

Wind loads depend on a lot of parameters of which changing one could lead to a significantly different result. To better monitor building behavior in the atmospheric boundary layer, achieving the best match boundary layer in BLWT is critical. The building model also plays a key role in the overall accuracy of the simulation. BLWT having long test sections allows boundary to grow fully and become the best match of the atmospheric boundary layer at a particular scale (Kopp et al., 2005^a). To have better tap resolution it's common to have a larger scale. However, a larger geometry scale could lead to a mismatch in the integral scale. It's commonly recognized by the wind engineering community that a balance should be achieved between large scale flow simulation and a larger building model. The balance should be constrained by two criteria, which are blockage of wind tunnel be less than 5% and the integral scale of turbulence be within a factor of two. Considering the objective of capturing detailed spatial pressure variation, a model scale of 1:18 was selected. At a model scale this large, it's hard to maintain the proper boundary layer scaling within the wind tunnel.

3.2.1 Model Geometry

The building model is shown in the Fig 3.2.1 and Fig 3.2.2. The building surfaces are made of clear polycarbonate plates which are rigid and impact resistant. It consists of two parts, the inner core, and outer surface panels. To form parapets, four stepper motors were installed at corners below wall panels. The outer wall can rise above the roof level with inner core remains at the same level (Whiteman et al., 2017).



Fig 3.2.1 Isometric view of Building Model (Left).
Adapted from ‘Optimization In Wind Engineering Using Cyber-Physical Systems For The Design Of Parapet Walls’ (Whiteman et al., 2017)



Fig 3.2.2 Front View of Building Model inside BLWT.
Adapted from 'Optimization In Wind Engineering Using Cyber-Physical Systems For The Design Of Parapet Walls' (Whiteman et al., 2017)

To accommodate the size of the turntable, the length of the building model was limited to 40 inches. To compare with previous studies, the length to width ratio of 3:2 was assigned to model. Therefore, the building model was assigned a plan dimension of 29.25 inches by 19.5 inches. By actuating outer walls, parapets of up to 5 inches was formed with a thickness of 1 inch. The building model has a flat roof and a height of 26 inches with parapet raised fully above the roof. Based on 1:18 scaled model dimensions, the full-scale dimension of the building was 44.5 feet by 29.6 feet by 30 feet. The thickness of the parapet is 18 inches in the full-scale model which satisfies the ASCE standard.

3.3 Result Processing

3.3.1 Data Resource

The experiments data are publicly accessible through the Natural Hazard Engineering Research Infrastructure (NHRI) DesignSafe cyberinfrastructure web-based research platform. Data output for each test configuration includes time-stamped Scanivalve pressure tap readings, pitot pressure, atmospheric data, cobra probe data, boundary layer profile, etc. The experimental dataset comprised of 288 data files in total. For each of the 6 parapet height, 24 data files were containing cumulative pressure information with the model rotated from 0° to 360 for every 15°.

3.3.2 Tap Distribution

The surface panels were instrumented with 512 pressure taps, out of which 334 taps were located on the roof. The tap distribution for the model with a parapet of 5 inches is shown in Fig 4.1.1. Surface 1, 2, 3 and 4 were the outer surface of walls around the perimeter of the building model. Surface 6, 7, 8 and 9 were the top section of the inner surface of walls. Surface 10 modeled by inner core represents roof. As indicated in the Fig 3.1.1, pressure taps were densely placed on the roof and loosely placed on wall panels. Around the corner of upwind edges, densely distributed taps monitored subtle pressure variation to capture the peak suction force. The pressure was measured by the acquisition system, Scanivalve ZOC33 pressure scanners. A total of 6 Scanivalve were used in test and each of them has 64 pressure inputs. Each of 64 inputs was connected to a corresponding pressure tap through Urethane tubing. Pressure for all taps were measured simultaneously and sampled at 625 Hz for 120 s.

This corresponds to pressure data collected at a wind speed of 40 m/s for 660 s assuming a velocity scale of 1/3.33. Pressure data digitally low-pass filtered at 200Hz and high-frequency components were blocked from being recorded into time history.

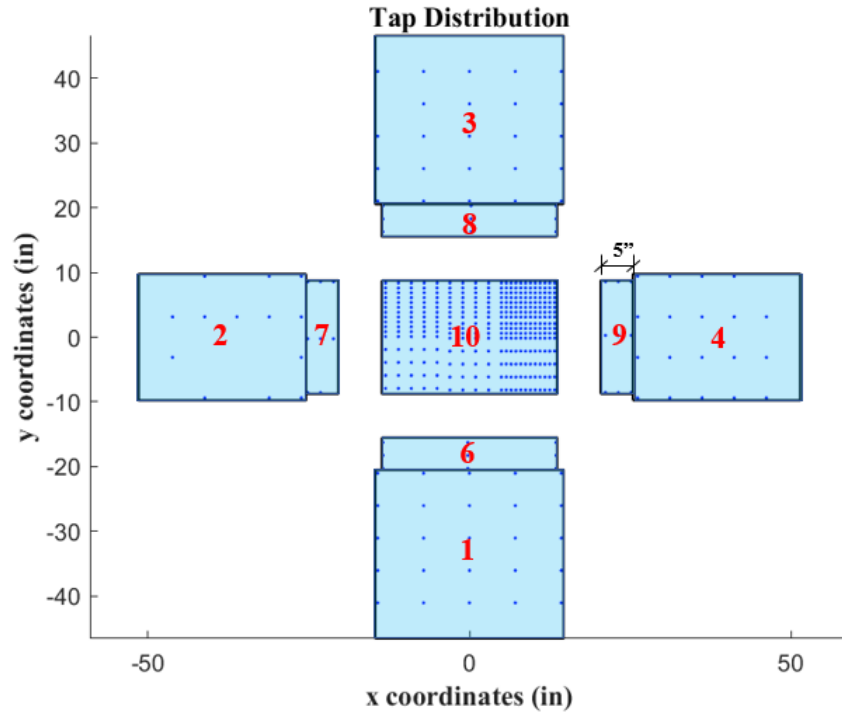


Fig 3.1.1 Tap distribution on surface panels of the building model.

Table 3.1 Details of Measurement configurations and data acquisition

Plan dimensions, W x L	9m x 13.6m (29.6ft x 44.5ft)
Eave height, H	9.1m (30ft)
Parapet heights	0, 0.45, 0.9, 1.8, 2.3m (0, 1.5, 3, 6, 7.5ft)
Upstream terrain roughness, Z_0	0.03m (0.0984ft)
Wind angles(deg)	0, 15, 30, ..., 330, 345
Number of Taps	512
Sampling frequency	625 Hz
Low pass filter cut-off frequency	200 Hz
Sampling time	120s
Reference wind tunnel speed	14 m/s
Model scale	1:18

3.4.2 Pressure Coefficient

The pressure coefficient (C_p) is commonly used to describe relative pressures throughout the flow field. It's one of the similarity parameters that make it independent and dimensionless to represent quantitative characteristics of physical similarity. (Anderson, 2011) That's the reason for choosing it to evaluate the effect of wind turbulence on a full-scale building through measurements from the scaled model. C_p is computed in the following equation as the ratio of relative static pressure at designation height to dynamic pressure at eave height.

$$C_p = \frac{P_0 - P_\infty}{\frac{1}{2} \rho_\infty v_\infty^2}$$
$$v_\infty = kU_H$$

Where P_0 (lb/in^2) is measured mean velocity pressure at the desired height. P_∞ (lb/in^2) is stagnation pressure at eave height in freestream. ρ_∞ (kg/m^3) is air density. v_∞ (m/s) is mean velocity at eave height.

To prevent disturbance due to embedment of pitot tube in freestream, mean eave height velocity (v_∞) was not measured directly at eave height. It was calculated indirectly by applying an empirical adjustment factor (k) to reference velocity (U_H). Flow measurements were taken at the various height using an automated gantry system equipped with Cobra probes that detects 3 components of velocity (u, v, w) and static pressure. Reference velocity was measured to be 15.4 m/s at a height of 1.48 meters with a model removed from the tunnel. Imperial adjustment factors (k) were calculated as $k = v_{1.48m}/v_i$. Plotting measured velocity components at varies height yields the mean velocity profile. Air density (ρ_∞) was calculated from the air

temperature, barometric pressure, and relative humidity measured during each test (Fernández et al., 2018).

Pressure time-history series were transformed into C_p time-history series. Average, RMS, Min and Max values were solved to characterize C_p . To identify the Minimum pressure coefficient $C_{p,Min}$ and the Maximum pressure coefficient $C_{p,Max}$ on the building model, Gumbel distribution was generated to model the distribution of the extreme value of C_p from the time history series for each tap. A time series was truncated into N segments and the segmental minimum/maximum value was identified. Out of N identified minimum/maximum values, a distribution of extreme value was generated. The 78th percentile of each distribution for $C_{p,Min}$ and $C_{p,Max}$ was used to determine the global extreme in the record.

Chapter 4: Experiment Results and Discussion

In chapter 4, the experiment result was validated by comparing the pressure distribution on the rooftop with/without parapet with pioneer researcher's studies. In chapter 6.3, Furthermore, the envelope of pressure distribution on the rooftop was compared with ASCE 7-16 by comparing converted C_p to the codified values of GC_p of the same building model. The measured pressure coefficients were consistent with that from ASCE 7-16.

4.1 Experimental Result Validation

4.1.1 Pressure Distribution on Rooftop without Parapet

As previous researchers have demonstrated for low rise buildings compacted with quartering wind, pressure distribution on the roof is comprised of highly loaded corners, highly loaded windward edges and lightly loaded interior areas. To validate the upwind characteristic's effect on experiment results, the distribution pattern of pressure was checked for discrepancies. Based on measurements of nearby taps, $C_{p,Min}$ for regions between taps were linearly interpolated and used to create contour maps. The contour map plotted at a wind angle of 45° and 0-inch parapets were shown in Fig 4.1.1. The pattern of pressure distribution agrees with those from previous studies. The experiment successfully described the behavior of airflow across the rooftop of a low-rise building.

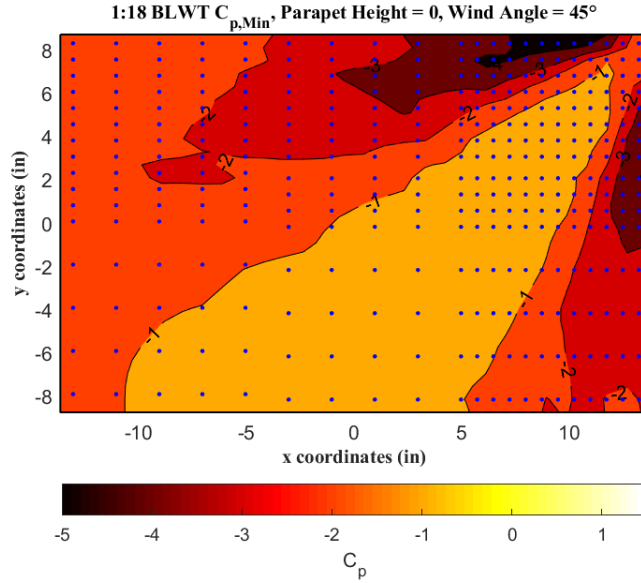


Fig 4.1.1 The distribution of $C_{p,Min}$ on roof of building model with 0" parapet

4.1.2 Pressure Distribution on Rooftop with Parapet

The pressure coefficients on roof surface protected by perimetric solid parapets were plotted below. Fig 4.1.2 to 4.1.6 shows $C_{p,Min}$ on the roof surface with 1" to 5" of parapet height. The mitigation effect of parapet can be best observed by the trend of the vortex's footprint. When conical vortices travel parallel along a surface, the separated shear layers can be very unstable and turbulent, and it will create strong suction forces on the nearby surface. From the figures, it can be observed that the dark red regions indicating high suction load shifted toward the bottom left corner as parapet height increase. The presence of parapet helped increasing $C_{p,Min}$ by deviating conical vortices away from the roof surface. As the parapet height increase, the $C_{p,Min}$ on the roof tap increase. The pattern was visibly changed for the case with 1" and 2" parapet, and it became milder and less obvious for a large area.

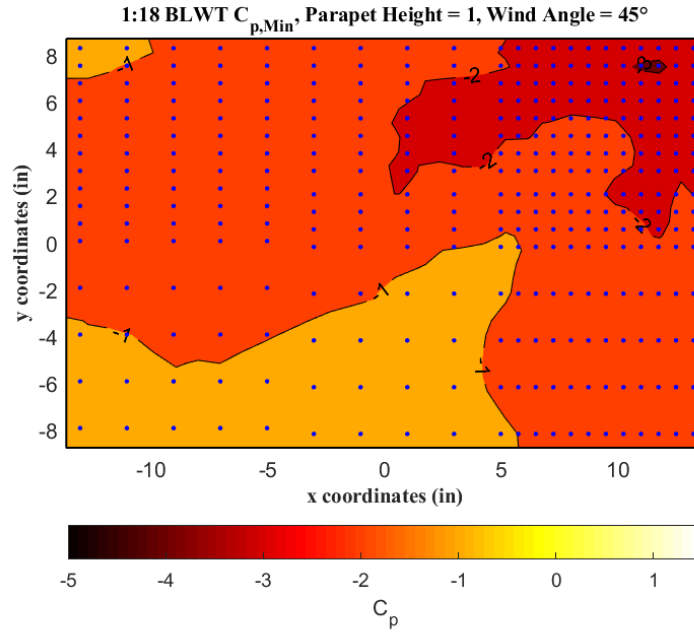


Fig 4.1.2 The distribution of $C_{p,Min}$ on roof of building model with 1" parapet

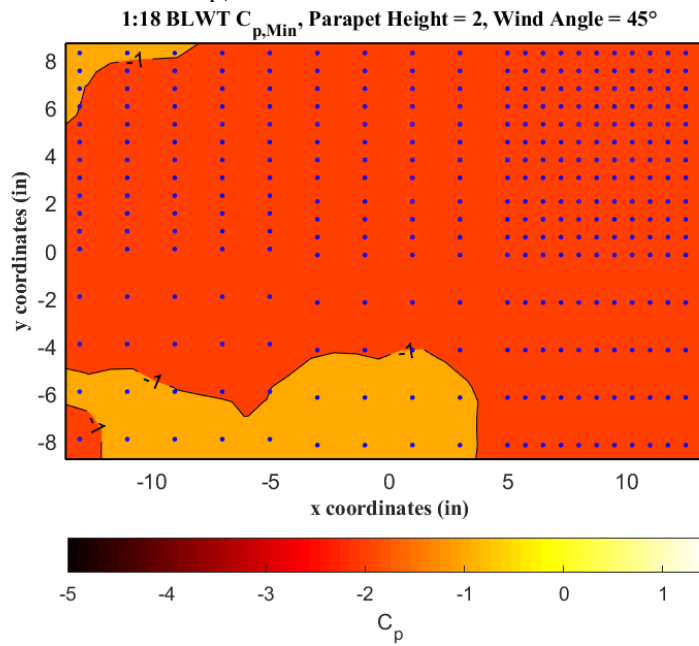


Fig 4.1.3 Distribution of $C_{p,Min}$ on roof of building model with 2" parapet

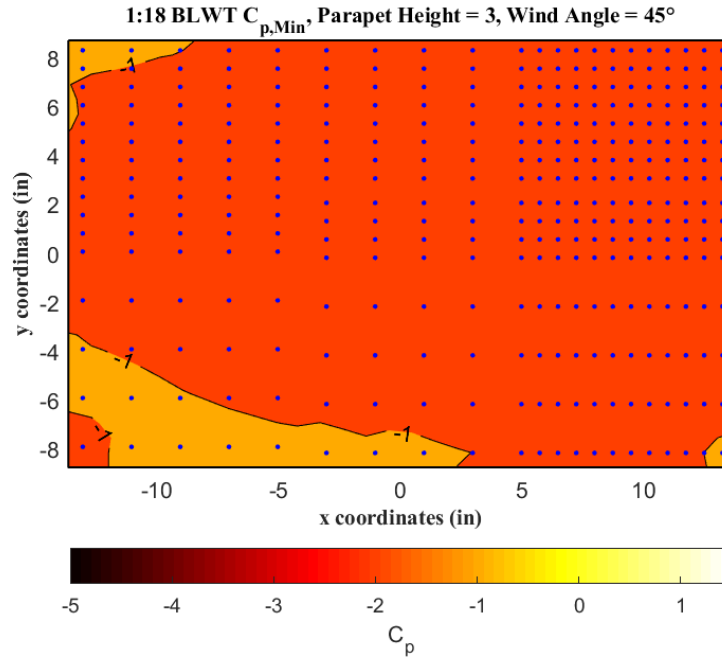


Fig 4.1.4 Distribution of $C_{p,Min}$ on roof of building model with 3" parapet

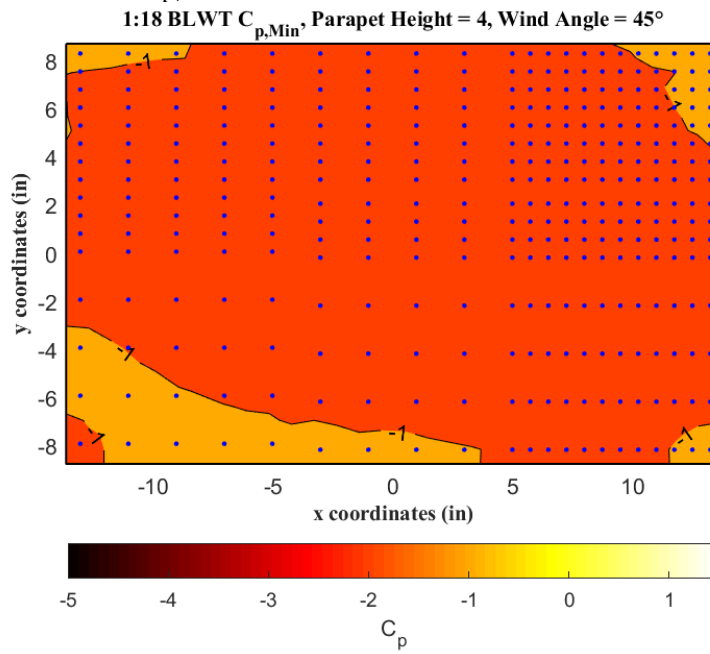


Fig 4.1.5 Distribution of $C_{p,Min}$ on roof of building model with 4" parapet

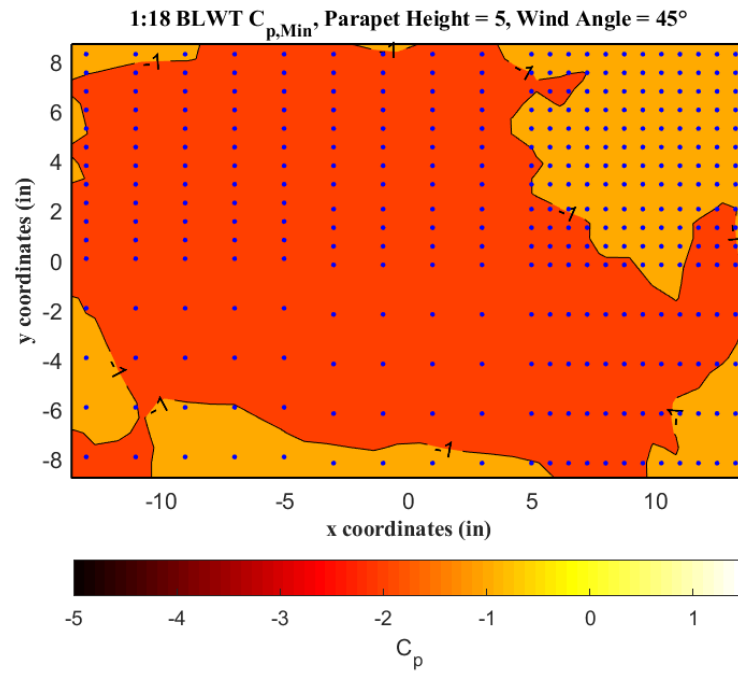


Fig 4.1.6 Distribution of $C_{p,Min}$ on roof of building model with 5" parapet

4.1.3 Mitigation Effect of Parapet on Rooftop

Parapet's effect on the mitigation of roof pressure was further investigated magnitude wise by solving for change in $C_{p,Min}$. Tap 132, 168 and 292 (Fig 4.1.7) selected from two windward edges and the interior area were evaluated for percentage reduction of peak suction. As shown in the Fig 4.1.8, increase of $C_{p,Min}$ by 5" parapet was up to 75% along the windward edge. As parapet height exceeds 3" the changing rate of $C_{p,Min}$ gradually decreased close to zero. The further increase of parapet height does not greatly affect the pressure pattern. The phenomenon agrees with Huang's research that concluded the reduction of peak suction (increase of $C_{p,Min}$) grows rapidly for $h/H < 0.15$ and became milder as the relative height of the parapet exceeds the threshold (Huang et al., 2017). Despite the reduction of peak suction along windward edges, the interior peak suction was drastically increased by 85% as a trade-off. Like taps near the windward edges and corner, the $C_{p,Min}$ of interior tap keeps decreasing as parapet become taller. Following the trend of these two patterns, an optimized parapet height would exist. At the optimized height, an objective function is minimized that factors in both decision variables of C_p . More detail about optimum parapet height is analyzed and discussed in detail in Chapter 6.2 as an application of ANN models.

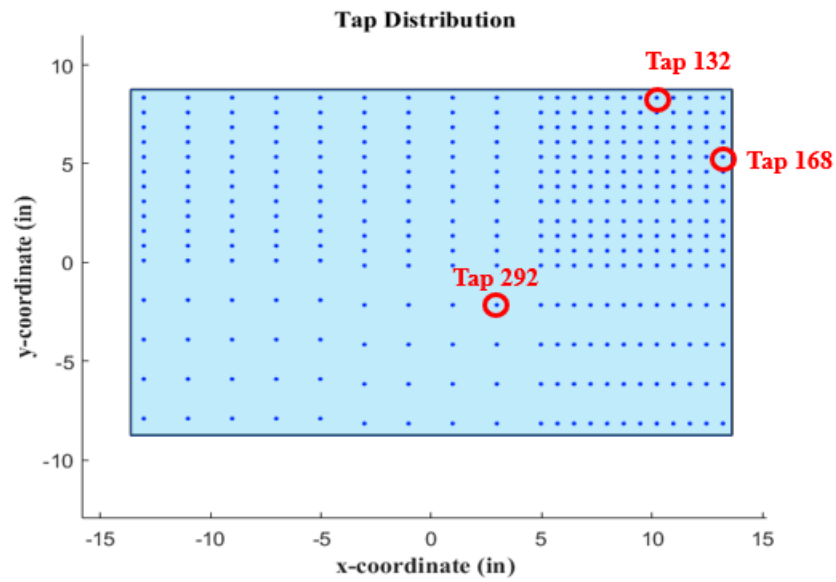


Fig 4.1.7 Location of Selected Tap 132, 168 and 292

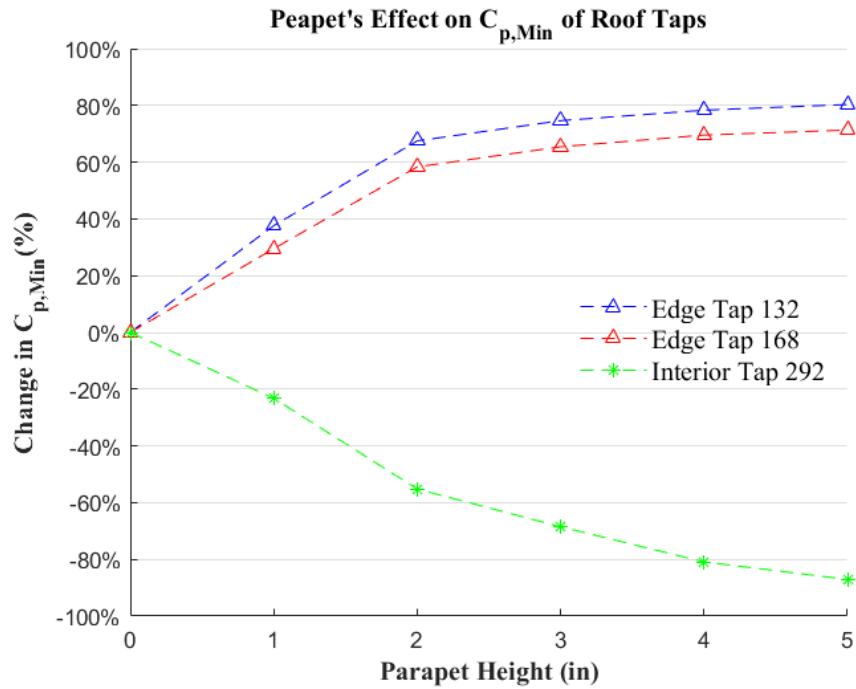


Fig 4.1.8 Parapet' effect on Minimum Pressure Coefficient of roof taps.

4.2 Experimental Result Validation by Comparison with ASCE

In Chapter 4.1 the experimental results were validated by comparing pressure distribution of the rooftop and percentage change in $C_{p,Min}$ with that from other researcher's conclusions. In this chapter, the $C_{p,Min}$ obtained from experiments were compared with the coefficients adopted in practical exercise from the current design code ASCE7-16. The experimental $C_{p,Min}$ were first converted into the same format used in ASCE that's equivalent to GC_p . Then based on the envelope of $C_{p,Min}$ from ASCE, the percentage difference in GC_p of a few representative taps were solved for comparison. The experimental results turned out to be mostly consistent with that from the ASCE. The small discrepancies in numerical values were due to inherent uncertainty and lack of large-scale turbulence. More details were discussed in Chapter 4.2.3.

4.2.1 Conversion of Pressure Coefficient C_p

The GC_p factor used in ASCE7-16 was pressure coefficients corresponding to 3-second gust wind speed at mean eave height. To compare coefficients with codified values, the result of wind tunnel test shall be converted into equivalent GC_p . The equation below was developed in Kopp's paper (Kopp et al., 2005^a).

$$(GC_p)_{eq} = \frac{q_H \hat{C}_p}{q_{10m,3s} K_{Zt} K_h K_d I} = F_{WT} \hat{C}_p$$

Where $(GC_p)_{eq}$ is the equivalent pressure coefficient corresponding to 3s gust wind speed, q_H is mean velocity pressure at eave height, $q_{10m,3s}$ is the 3-second gust velocity pressure at 10 m above ground, \hat{C}_p is pressure coefficients obtained from

wind tunnel test corresponds to 660s wind speed, K_{zt} is the topographic factor, K_h is the terrain factor, K_d is the directionality factor, I represent the importance factor of the structure. K_h is determined with Table 26.10-1 from ASCE7-16 which equals 0.98 at eave height for exposure category C. Both K_{zt} and K_d are assumed to be 1. The importance factor of an office is 1.

The equation can be further broken down into,

$$(GC_p)_{eq} = \frac{\frac{1}{2} \rho_{\infty} v_{h,660s}^2 \hat{C}_p}{\frac{1}{2} \rho_{\infty} v_{10m,3s}^2 K_{zt} K_h K_d I} = F_{WT} \hat{C}_p$$

The test duration at the model scale was 120s which corresponds to 660s at full scale.

$v_{h,660s}$ is the mean wind velocity at eave height h over 660 seconds of test duration.

$v_{10m,3s}$ is the 3-second gust velocity at 10m above ground. The two velocities at different height and different duration can be related by the intermediate-term. The 3s gust velocity at 10m can be converted to mean velocity $v_{10m,660s}$ at eave height h over 660s. The equation above can be further broken down into,

$$(GC_p)_{eq} = \frac{v_{h,660s}^2}{v_{10m,3s}^2} \frac{\hat{C}_p}{K_{zt} K_h K_d I} = \left(\frac{v_{10m,660s}}{v_{10m,3s}} \frac{v_{h,660s}}{v_{10m,660s}} \right) \left(\frac{\hat{C}_p}{K_{zt} K_h K_d I} \right)$$

The ratio $\frac{v_{10m,660s}}{v_{10m,3s}}$ was determined using the the Durst curve in Fig 4.2.1. From curve

readings at gust duration of 3s and 660s, $\frac{v_{10m,660s}}{v_{10m,3600s}} = 1.05$ and $\frac{v_{10m,3s}}{v_{10m,3600s}} = 1.52$ were

substituted into the equation that yields $\frac{v_{10m,660s}}{v_{10m,3s}} = 0.69$. To solve for the other

fraction inside the bracket, the mean velocity profile (Fig 4.2.2) was utilized which was constructed using flow measurements at different height with model removed.

The profile was normalized by reference velocity U_{ref} of 15.3 m/s at 1.48 m. At the

same velocity scale, the velocity ratio $\frac{v_{h,660s}}{v_{10m,660s}}$ at full scale equals velocity ratio

$\frac{v_{508mm,660s}}{v_{560mm,660s}}$ at model scale. The mean eave height velocity $v_{508mm,660s}$ equals 12.304

m/s. The mean velocity at 560mm $v_{560mm,660s}$ was interpolated from velocity profile

to be $v_{1.48m,660s} * U/U_{ref} = 15.3 * 0.82 = 12.55 \text{ m/s}$. The term $\frac{v_{h,660s}}{v_{10m,660s}}$ was

solved to be 0.98. Substitute all the previously obtained value into the equation yields

a coefficient F_{WT} of 0.69.

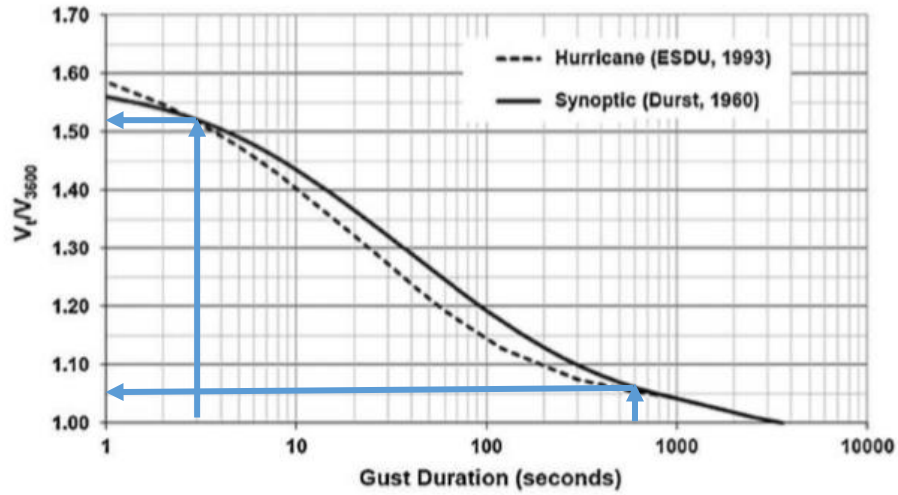


Fig 4.2.1. Durst curve.

Adapted from 'Minimum Design Loads for Buildings and other Structures' (ASCE, 2016)

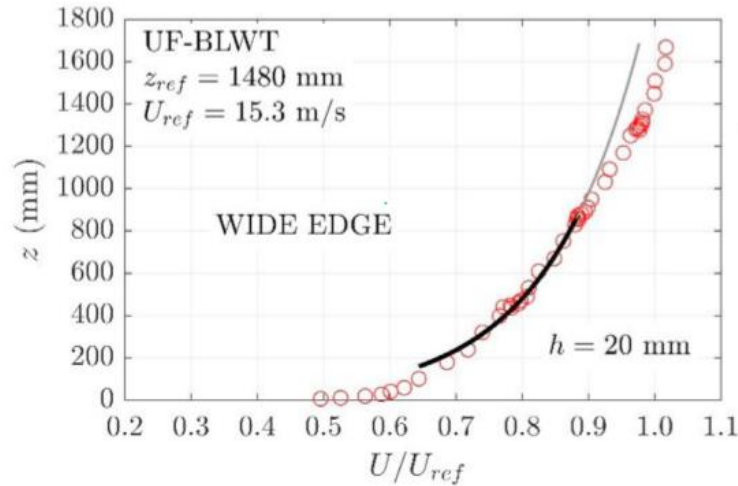


Fig 4.2.2 Mean Wind Velocity Profile obtained from Cobra Probe Measurements. Adapted from ‘Optimal design of structures using cyber-physical wind tunnel experiments with mechatronic models’ (Whiteman et al., 2017)

As described in Chapter 2.3, GC_p acting on building surfaces were obtained from ASCE 7-16 with applicable diagrams. The dependent variable is effective wind area which indicates GC_p are area-averaged coefficients. Components with a large surface area would be less likely to experience high local pressure and vice versa. Since the goal was to verify pressure distribution and magnitude with codified value, the effective wind area of the single tap was taken as 1 ft^2 .

Two load cases, windward parapet (load case A) and leeward parapet (load case B), were considered to determine the pressure for parapet walls. Since the 1:18 model has a small width (depth) to height ratio, the flow has been deflected far enough away from the roof that doesn't reattach. Therefore, the inner section of the leeward parapet wall would never experience positive pressure but a suction with a lower magnitude. Because shear layers are closer to windward-edge than leeward-edge, the suction near former is always higher than the latter. It's conservative to assume peak suction coefficient for all inner parapet wall are equal.

The GC_p on windward parapet (p1) was determined to be 1. The GC_p on leeward parapet (p2&p3) equals -2.3 and -3.2 corresponding to zone 2 and 3. The GC_p on Leeward suction load (p4) equals -1.1 and -1.4 for zone 2 and zone 3. These values are enveloped to eliminate wind directionality, and the negative values are the minimum pressure coefficients among all wind angles. The corresponding GC_p to each surface was plotted in the Fig 4.2.3.

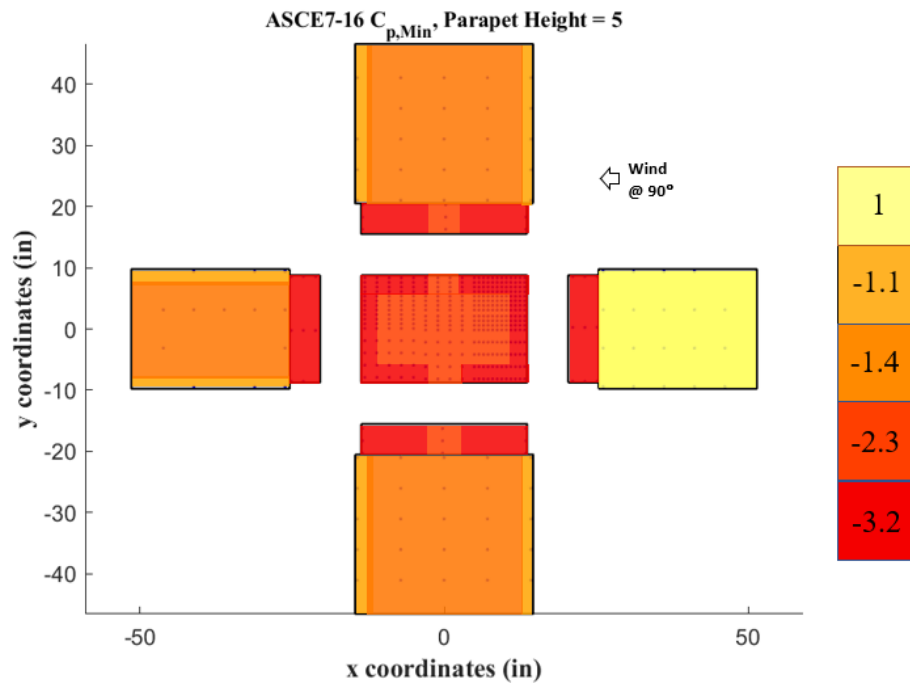


Fig 4.2.3 Envelop of pressure coefficients through ASCE7-16 on low-rise building

4.2.2 Discrepancy between Equivalent GC_p and GC_p from ASCE7-16

From experiment measurements of pressure on the low-rise building, the $C_{p,Min}$ within a time series was obtained through Type 1 Gumbel distribution on each tap at 24 angles and 6 parapet heights. At the same parapet height, there're 24 of $C_{p,Min}$ for every single tap. Out of these 24 values, a global minimum value of $C_{p,Min}$ was selected to represent the most severe condition possible, and the angles at which the minimum $C_{p,Min}$ were selected are not essentially the same. Then, the F_{WT} was factored into the $C_{p,Min}$ to obtain equivalent GC_p . In Fig 4.2.4, a Voronoi diagram was used to plot the envelope of the minimum equivalent GC_p from BLWT experimental results. The diagram was constructed based on Delaunay triangulation for a set of points. The surface plane was partitioned into multiple small cells inside which a tap is located equally distanced to edges of the cell. The diagram was used to analyze $C_{p,Min}$ of a region from spatially distributed taps. The envelope of equivalent GC_p on the roof is shown in the Fig 4.2.4.

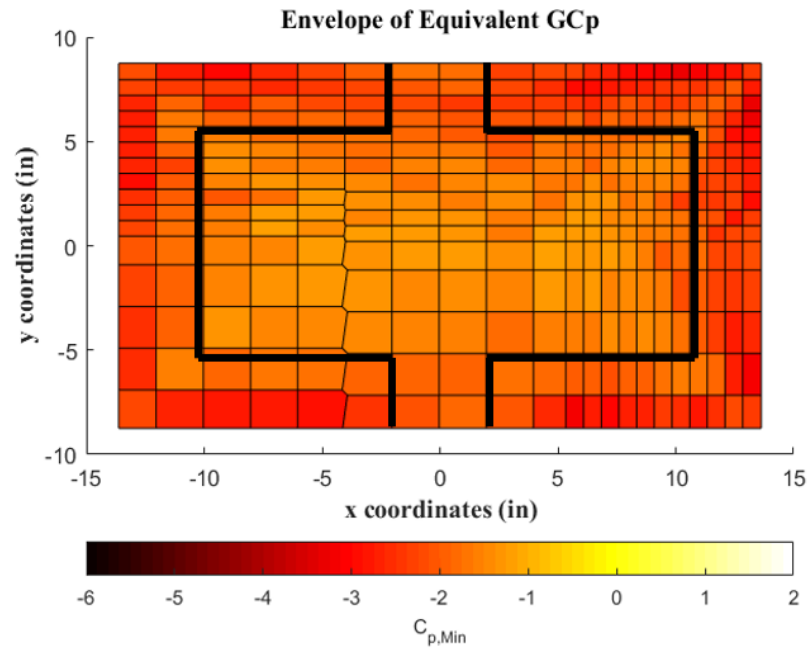


Fig 4.2.4 Envelope of Equivalent GC_p on roof by Voronoi Diagram

4.2.3 Discussion on Identified Discrepancy

The number of cells equals the number of roof taps. The minimum GC_p were obtained at parapet height of 0". Due to the non-uniform distribution of roof taps, the Voronoi cells in regions with densely distributed taps were smaller in size and vice versa. The low resolution may result in an inaccurate presentation of pressure pattern near the bottom left corner. The darker red regions were mostly along the four edges and the interior region was lightly colored. The pattern was then compared to that expected from using ASCE 7-16. By closely observing the interior region, it's clear that GC_p is not uniform but rather increasing moving towards the center. The footprint of conical vortices is visible at four nearly symmetrical corners. The inner pressure distribution of inner parapets follows the pattern of the near roof edge. It's consistent with parapet loading from ASCE 7-16.

The exposed portion of leeward parapets experienced suction during the whole test, which was inconsistent with the ASCE. The scale of the building model may be contributed to the difference. The height to length ratio of the building model was 1:1 which means limited length for the shear layer's reattachment. The separated shear layer never reattaches to the roof surface before leaving the model boundaries. Small discrepancies were found in comparison to the min GC_p from ASCE magnitude wise. The minimum GC_p along edges and corners is -3.31 which is 3.4% lower than -3.2 from ASCE. The minimum GC_p the interior region is -2.37 which is 3% lower than -2.3 from ASCE. There could be a list of reasons that possibly caused the difference. As discussed previously, the longitudinal integral length L_x doesn't meet the standard from ASCE/SEI 49-12. The L_x of the simulated terrain, the condition

was solved to be 18 m at eave height which was very low compared with the codified value of 110 m. Another reason is the inherent uncertainty when using Gumbel distribution to estimate the minimum values.

4.3 Sheltering Effect of Parapet on the Rooftop

Parapet's mitigation effect is most visible on the building roof at 45° which causes the highest suction load among all angles. While most researchers have focused the wind effect at the most severe condition, the mitigation effect on the rooftop at non-oblique angles is seldomly mentioned. In this chapter, the reduction of $C_{p,Min}$ were investigated for the relationship with parapet height. Besides, the pressure distribution over the surface panels were plotted by contour maps. When wind impacts the building surface at right angles, the pattern of roof pressure distribution becomes simpler due to the absence of conical vortices. The pressure distribution on the roof is generally uniform with a few minor variations. To investigate the effect of parapets on the roof at non-oblique angles, contour maps of $C_{p,Min}$ on surfaces were plotted at 0° and 90° with 0"-5" parapet.

4.3.1 Sheltering Effect at 0° wind (along the short dimension)

Fig 4.3.1 to 4.3.6 shows $C_{p,Min}$ of all surfaces at an angle of 0° and parapet heights from 0" to 5". As shown in the series of figures, the parapet lower than 4" doesn't change the flow pattern enough to post a noticeable effect on the roof pressure. Even with taller parapets, most of the roof taps were exposed to turbulence flow and experienced high suction pressure. Only the middle part of windward edges was sheltered by parapets for about 2" down the roof. The increase of $C_{p,Min}$ was around 18% which's only one-fourth of that at the wind angle of 45° . The parapet is not so effective in this type of wind condition. The design is dominated by wind pressure at the wind angle of 45° .

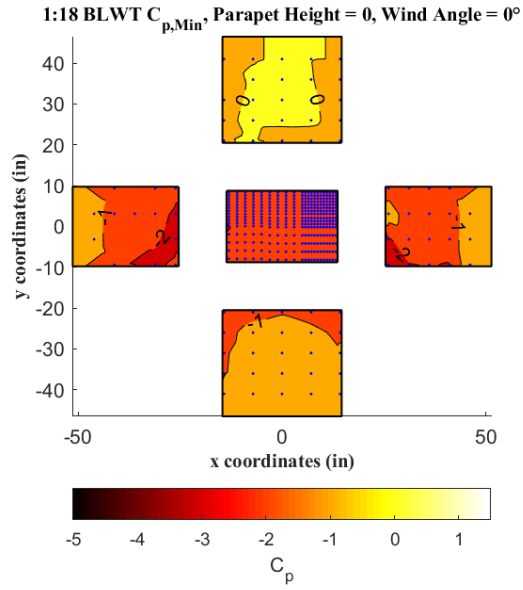


Fig 4.3.1 Pressure distribution contour from experiment result at 0" parapet and 0° wind angle.

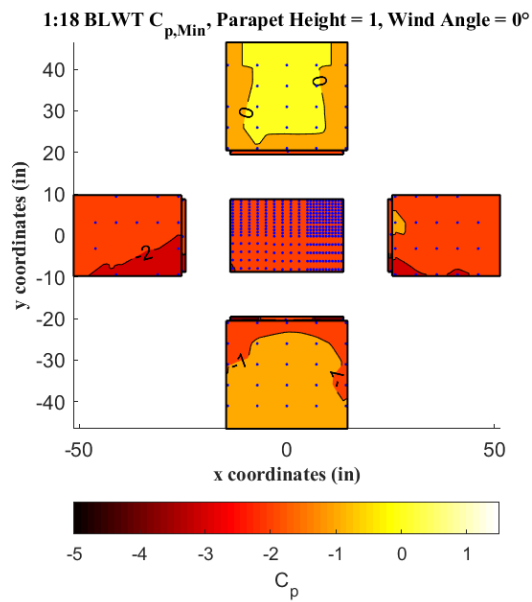


Fig 4.3.2 Pressure distribution contour from experiment result at 1" parapet and 0° wind angle.

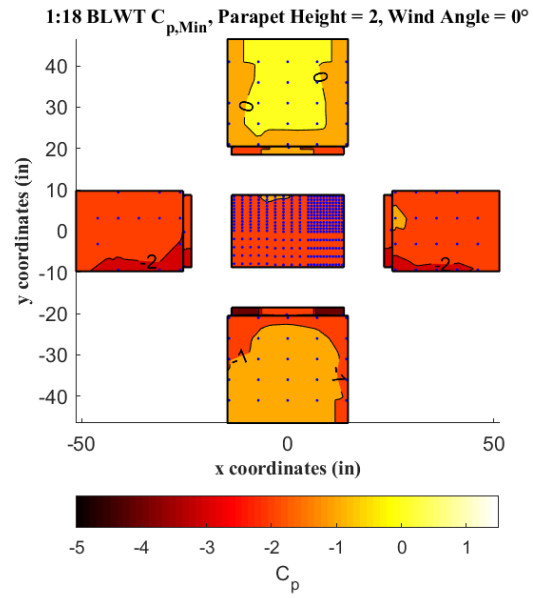


Fig 4.3.3 Pressure distribution contour from experiment result at 2" parapet and 0° wind angle.

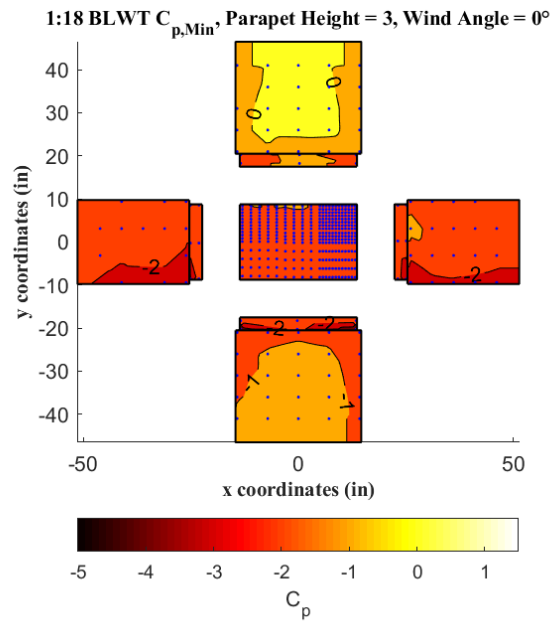


Fig 4.3.4 Pressure distribution contour from experiment result at 3" parapet and 0° wind angle.

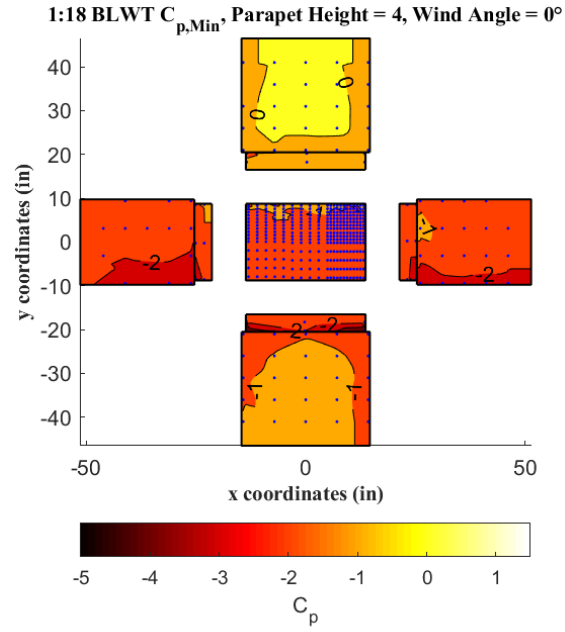


Fig 4.3.5 Pressure distribution contour from experiment result at 4" parapet and 0° wind angle.

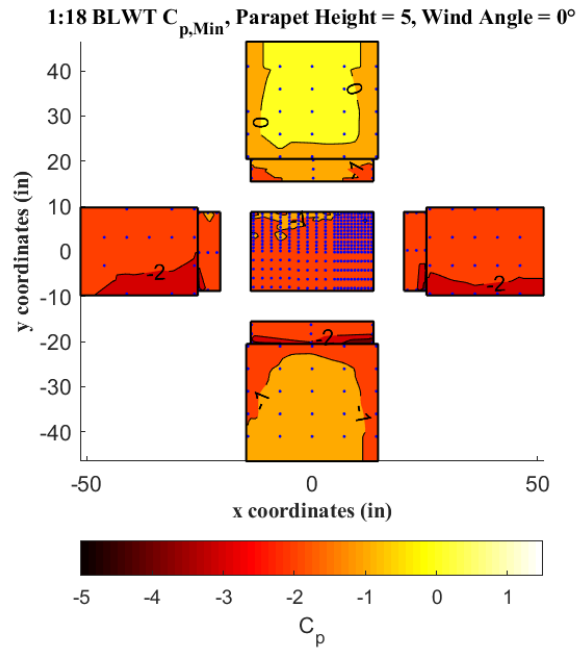


Fig 4.3.6 Pressure distribution contour from experiment result at 5" parapet and 0° wind angle.

4.3.2 Sheltering Effect at 90° wind

Similarly, the pattern for $C_{p,Min}$ were plotted and shown below in Fig 4.3.7 to 4.3.12. The mitigation effect is more obvious when the building model is at 90° to the approaching flow. As parapet height increase, $C_{p,Min}$ increases near the roof region along the windward edge. The mitigation effect is most obvious at the parapet of 5". At the taps right next to the windward edge, an increase of the $C_{p,Min}$ is 32% which is less than one-half of the increase at the wind angle of 45°. Despite the degree of mitigation effect at 90°, nearly 1/2 of the roof surface was sheltered by the windward parapet. The sheltering effect is considerable compared to the building model that's subjected to at 0° wind.

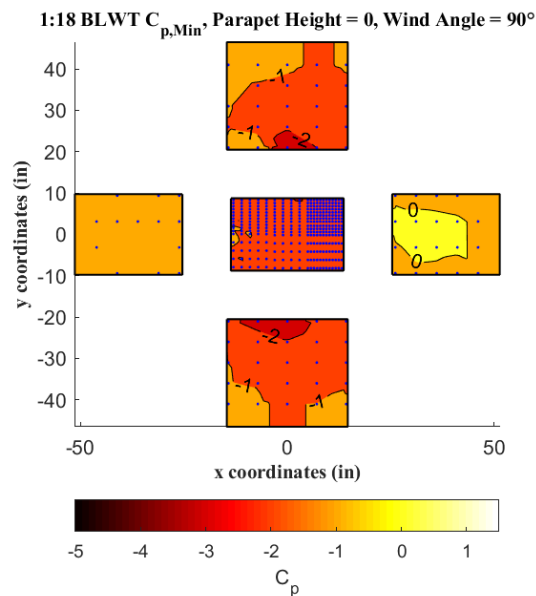


Fig 4.3.7 Pressure distribution contour from experiment result at 0" parapet and 90° wind angle.

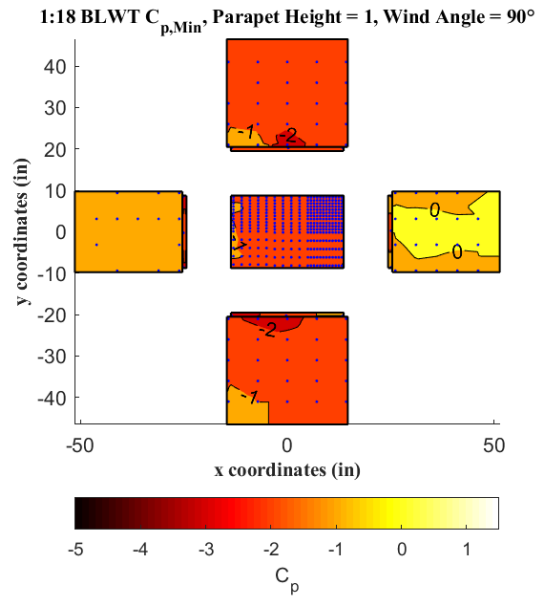


Fig 4.3.8 Pressure distribution contour from experiment result at 1" parapet and 90° wind angle.

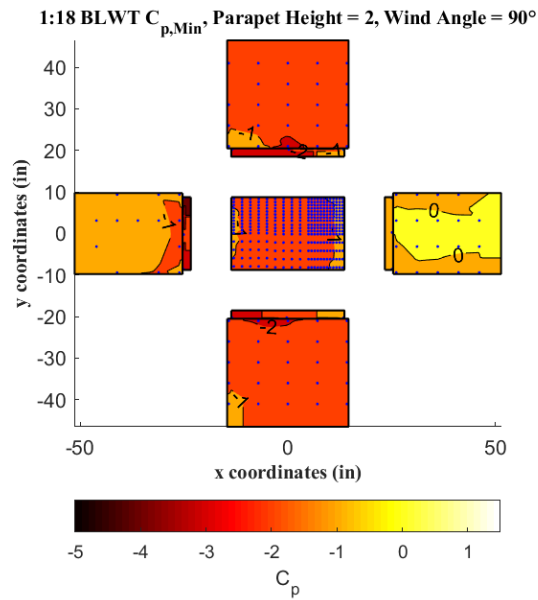


Fig 4.3.9 Pressure distribution contour from experiment result at 2" parapet and 90° wind angle.

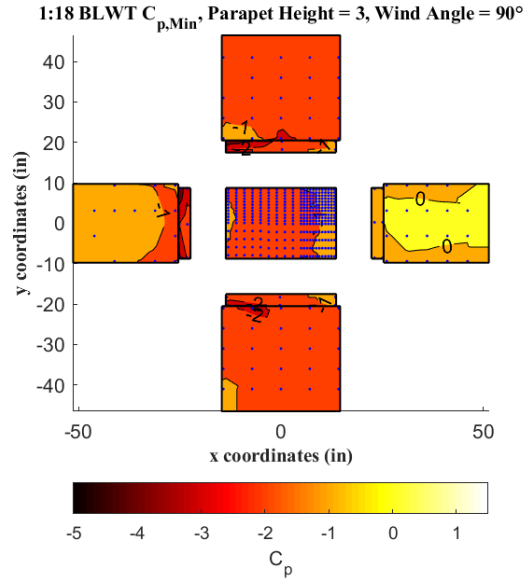


Fig 4.3.10 Pressure distribution contour from experiment result at 3" parapet and 90° wind angle.

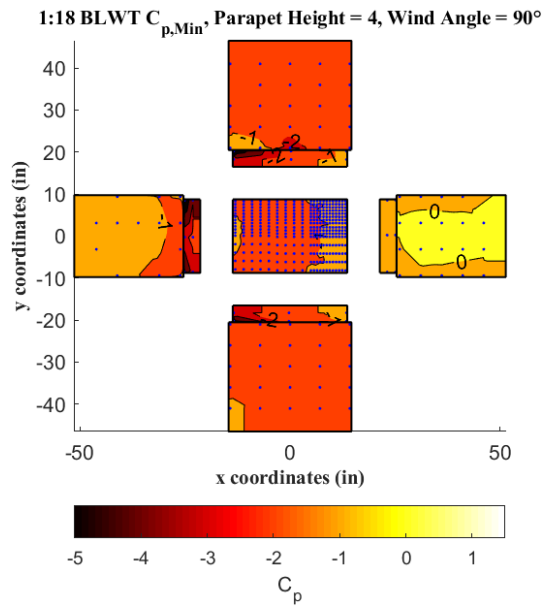


Fig 4.3.11 Pressure distribution contour from experiment result at 4" parapet and 90° wind angle.

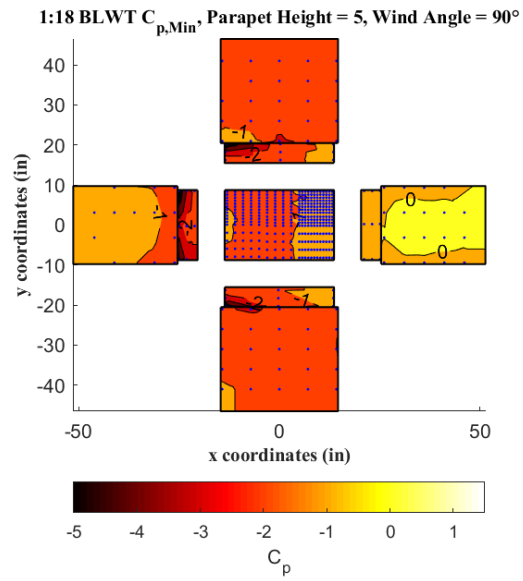


Fig 4.3.12 Pressure distribution contour from experiment result at 5" parapet and 90° wind angle.

4.3.3 Discussion on Mitigation Effect of Parapet

From the two cases investigated above, two different responses were observed on the roof of the same model due to different wind directions. In the first case where the long edge was facing the approaching wind, the parapet made subtle influences on the distribution pattern of the roof $C_{p,Min}$. Whereas in the other cases when the short edge was facing the wind, considerable changes on pattern of the roof $C_{p,Min}$ were observed. There're two conclusions regarding the parapet's effect on the roof that can be made. The first one is that the taller the parapet, the better the sheltering effect is. The second one is that the sheltering effect of the parapet was related (negatively proportional) to the length of the windward edge.

Tall parapets helped mitigated the roof wind loading. The reasoning of mitigation is demonstrated below. The parapet made separated shear layers to deviate away from the roof. As shown in Fig 4.3.13, the curvature of shear layers was lessened so that it reattaches further down the roof. The deviated shear layers can be described by a concave-down parabolic curve. As parapet height starts to increase, the larger distance between the roof and shear layers resulted in the increase of $C_{p,Min}$ near windward edges. It's also worth noting the $C_{p,Min}$ of windward inner parapet also increased along with sheltered roof regions. Meanwhile, the $C_{p,Min}$ for upper regions of the leeward parapet was reduced because getting closer to the shear layers yields strong suction.

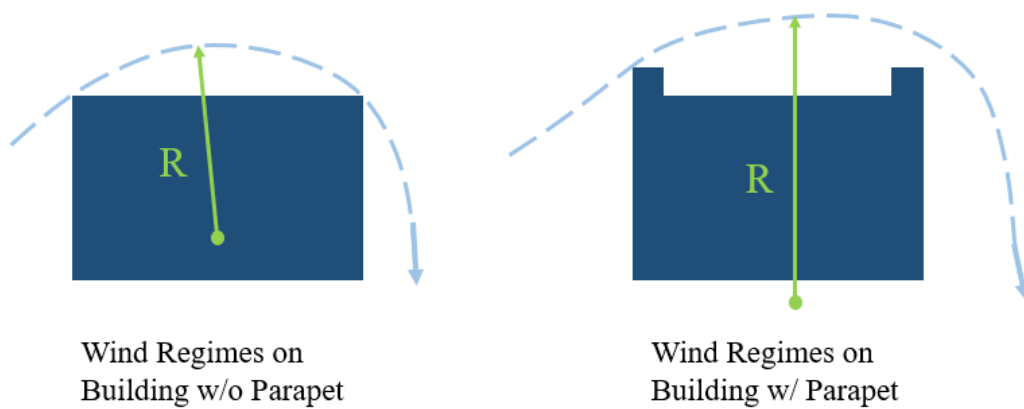


Fig 4.3.13 Curvature of Shear Layers on Building Models with (Right) and without (Left) Parapets.

The response for roof $C_{p,Min}$ at 90° can be explained by the theory above whereas in the first case at the wind angle of 0° doesn't seem to abide by the same concept. Although, parapet helped with alleviating shear layers in both two cases. The mitigation effect on the long edges is insignificant compared with than on the short edges. The mitigation effect seems to be negatively proportional to the length of the windward edge. Recall the wind regime on low-rising building in Fig 2.2.1, the width of the separation zone is non-uniform along the windward edge. It peaks at the center and decreases as it reaches the two ends. The shear layer near the center region is blocked by the parapet completely and must ride over the parapet. Whereas the shear layer near both ends could escape from the side. With the same amount of energy of approaching wind, it's easier to ride over a parapet along a shorter edge than longer one. separation zone became more distributed along the longer edges.

Chapter 5: Artificial Neural Network Setup

ANNs have broad applications throughout many industries including wind engineering applications. Artificial neural networks can learn and model any non-linear relationship between inputs and outputs without complex statistics. The model could process a massive amount of overserved data and uncovers the underlying function. The network model provides a user with a ‘black-box’ system that’s used to conveniently predict outputs with given inputs.

In this study, three models were developed to predict the wind pressure coefficients C_p on the low-rise building. The fully trained model can be used to extend database. For example, the model can extrapolate C_p on building model at different unseen parapet height and angle.

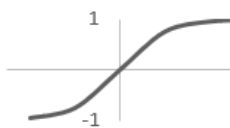
5.1 Data Division

Pressure time-history was obtained for taps on the roof, inner parapets, and outer walls. There’s a total of 48383 data points representing pressure coefficients on the roof. The data points are from measurements on 336 taps at 24 different angles and 6 parapet heights. On the inner parapet walls, the maximum number of exposed taps is 36. There’s a total of 2568 data points representing pressure coefficients at 24 angles and 6 heights. On the wall surfaces, the maximum number of exposed tap is 80. The total number of pressure coefficients for wall taps are 11664. The division of data for training, validation and testing was set to be random at a portion of 70-15-15 accordingly. Using randomly selected data has a minor effect on the performance of a well-developed model.

5.2 Network Architecture and Selection of Parameters

In a practical condition with unknown target function, the trends of E_{in} and E_{out} are unveiled and the best practice is using all available training data to develop complex networks and the model complexity should be pushed to the limit when out-of-sample error starts to increase. To decide the best architecture concerning costs and performance, multiple trial configurations for network architecture were tested for the generalizing ability of the ANN model. Based on the different behavior of structural components to wind load, 3 neural network models were developed separately for the roof, parapets, and wall surfaces. In this research, the structure of a four-layer feed-forward network was employed with 1 input, 1 output, and 2 hidden layers. The neurons in each hidden layer were adjusted according to generalization performance. The detailed structures of proposed ANN models were specified in Table 5.1.

Table 5.1 ANN Model Characteristics

Inputs	x, y, h, θ, z		
Outputs	$C_{p,mean} \ C_{p,rms} \ C_{p,Min} \ C_{p,Max}$		
ANN Structure	Roof BP 5-60-10-4		
	Walls BP 5-95-15-4		
	Parapet BP 5-95-15-4		
Transfer Function	Hyperbolic tangent		
	$\theta(s) = \frac{e^s - e^{-s}}{e^s + e^{-s}}$		
Wind Direction, θ	from 0 to 360 for every 15 degrees		
Data Division	Training: Validation: Testing = 70:15:15		
Training Algorithm	LM and BR Backpropagation		
Number of Validation Checks	6		
Training Performance Gradient	0.001		

Pressure coefficients on the building surface depend greatly on the location of the tap. The training parameters for both models are identical including x, y, z coordinates of tap, parapet height and wind angle. Because roof taps are on the same level, the z coordinates for 48383 yields a row of constant parameters. The row does not contribute to output's convergence to the true value, and it was removed by preprocessing function implanted in MATLAB code before training occurs. Many researchers include turbulence intensity as a training parameter because fluctuating and peak external pressures are highly dependent on the turbulence intensities (Holmes, 2001). However, it's not selected as an input parameter as only one terrain roughness was simulated yielding the same turbulence intensity at eave height. There are four outputs namely Mean, RMS, Min and Max pressure coefficient. They were used to measure the general level of pressure fluctuations at taps.

5.3 BP Algorithm Selection

BP algorithm can be categorized into seven parts: 1) Adaptive Momentum 2) Self-adaptive learning rate 3) Resilient BP 4) Conjugate Gradient 5) Quasi-Newton 6) Bayesian regularization 7) Levenberg Marquardt. Table 5.2 is a portion of the BP algorithm available in MATLAB.

Table 5.2 Types of Backpropagation Algorithm.

MatLAB Function Name	BP Algorithm
trainbfg	Quasi-Newton
traincgf	Fletcher-Powell Conjugate gradient
traincgp	Polak-Ribiere Conjugate Gradient
traingd	Gradient Descent
trainlm	Levenberg-Marquardt
trainscg	Scaled Conjugate gradient
trainbr	Bayesian Regularization

Adapted from ‘Deep Learning Toolbox’, 2020, MATLAB Documentation. Copyright 2020 The Mathworks, Lnc.

In this study, Levenberg-Marquardt and Bayesian Regularization backpropagation were utilized for its ability to approach second-order training speed. Both LM and BR backpropagation utilizes Levenberg-Marquardt optimization to update the weight and bias values. Different than the LM-BP, the BR-BP minimize a combination of squared errors and weights and optimize the network generalization performance by determining the correct combination (MATLAB documentation). It’s proven in Pan's (2013) research on the comparison between different types of BP algorithm that BR is the preferred algorithm for its lowest mean absolute percentage error of 3.5% (Pan et al., 2013). Whereas BR possesses the highest generalization ability, LM-BP is the fastest algorithm that produces MAPE within a tolerance range. For the generalization of the ANN model based on the measurement of roof taps, the

available data input for training is relatively large and the LM backpropagation was selected to increase training speed. For wall and parapet taps, LM-BP was first used to train the network and later it was switched to BR-BP for better performance.

5.4 Termination Constraint

Both LM-BP and BR-BP use the number of iteration and max number of validation checks as termination criteria. As training terminates, the performance goal shall be infinitely close to 0 as the gradient is set to be below 10^{-7} . Max's number of iterations was set at 2000 to avoid overfitting and excessive training duration, and the max fail of validation is set at 6. Other Marquardt adjustment related parameters were set at default.

5.5 Chapter Conclusion

For each data subset of roof, parapet, and wall, 70% of data were randomly selected and fed into the raw network as a training guide. Coordinates of tap, the height of parapet, and wind angle were plug into the feedforward process as input. The output parameters were Mean, RMSE, Minimum, and Maximum of the C_p time-series of each tap. In the feedforward process, the product of weight and input were summed together and plugged into the sigmoid transfer function $\theta = \tanh(\sum s_i)$ as input for the next layer. After the feedforward process propagates through layers of nodes and reaches the output layer, the output vector will be compared with the target vector. If the difference between two vectors is within the tolerance range, the training of network terminates followed by weights and bias on each link being retained for future use. Utilizing backpropagation, the network weights were tuned to reflect the true value of the corresponding output. The network mainly operates on one of the two BP-algorithms including LM and BR backpropagation. BR backpropagation takes a longer time to train and generally yields better performance than LM backpropagation. The training terminates when validation error doesn't improve for 6 consecutive epochs. The combination of tuned weights and bias were saved for future use.

Chapter 6: Neural Network Results and Discussions

6.1 Performance Evaluation of ANN Model

6.1.1 Performance Evaluation by Linear Regression

After the network finished tuning and tested with the test subset, the output vector $h(x)$ was then being used to plot against the true value (y). Linear regression was used to model the relationship between ANN outputs and BLWT outputs. RMSE, MEAN, and R^2 were calculated to quantify the strength of the relationship as shown in following equations,

$$RMSE = \sqrt{\frac{1}{n} \sum_{i=1}^n (y_i - h(x_i))^2}$$

$$MAE = \frac{1}{n} \sum_{i=1}^n |y_i - h(x_i)|$$

$$R^2 = 1 - \frac{\sum_{i=1}^n (y_i - h(x_i))^2}{\sum_{i=1}^n (y_i - \overline{h(x)})^2}$$

Where y_i is the BLWT result, $h(x_i)$ is the ANN predicted result, $\overline{h(x)}$ is the mean value of BLWT result, n is the number of data points used in data subsets (train, validate and test).

The linear regression plot for each subset were plotted and shown in Fig 6.1.1 to 6.1.3. The relatively low RMSE and MAE means a very good agreement between observed results and predicted results. Therefore, a high degree of generalization is achieved. Also, the squared error for the training subset is the least among three subsets which demonstrated that model complexity is appropriate resulting in low in-

sample error. The other two subsets also have relatively low squared error indicating the overfitting was prevented by cooperating with validation sets. Table 6.1 shows MAE, RMSE, R^2 of each type of pressure coefficients for all three ANN models. In all three models, the $C_{p,Min}$ and $C_{p,Max}$ have larger MAE and RMSE compared to $C_{p,Mean}$, $C_{p,RMS}$. The more spread-out data points are due to uncertainties generated when estimating the maximum and the minimum using Gumbel distribution.

Table 6.1 Test Error for ANN models.

Surface Type	Pressure coefficient	MAE	RMSE	R^2
Roof	Mean	0.044	0.060	0.919
	RMS	0.040	0.055	0.916
	Min	0.085	0.122	0.859
	Max	0.072	0.100	0.924
Wall	Mean	0.053	0.074	0.967
	RMS	0.061	0.082	0.791
	Min	0.094	0.150	0.935
	Max	0.071	0.095	0.953
Parapet	Mean	0.076	0.101	0.820
	RMS	0.057	0.076	0.752
	Min	0.168	0.280	0.809
	Max	0.177	0.250	0.806

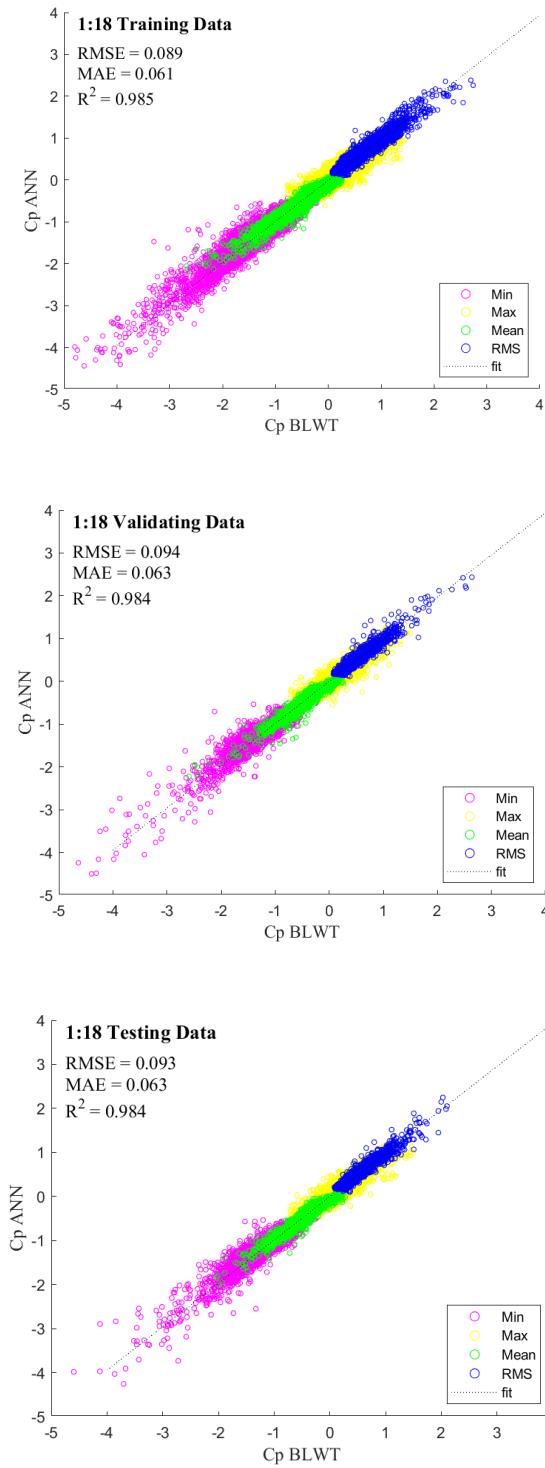


Fig 6.1.1 linear regression plots for training, validation and testing subsets of ANN model for the roof.

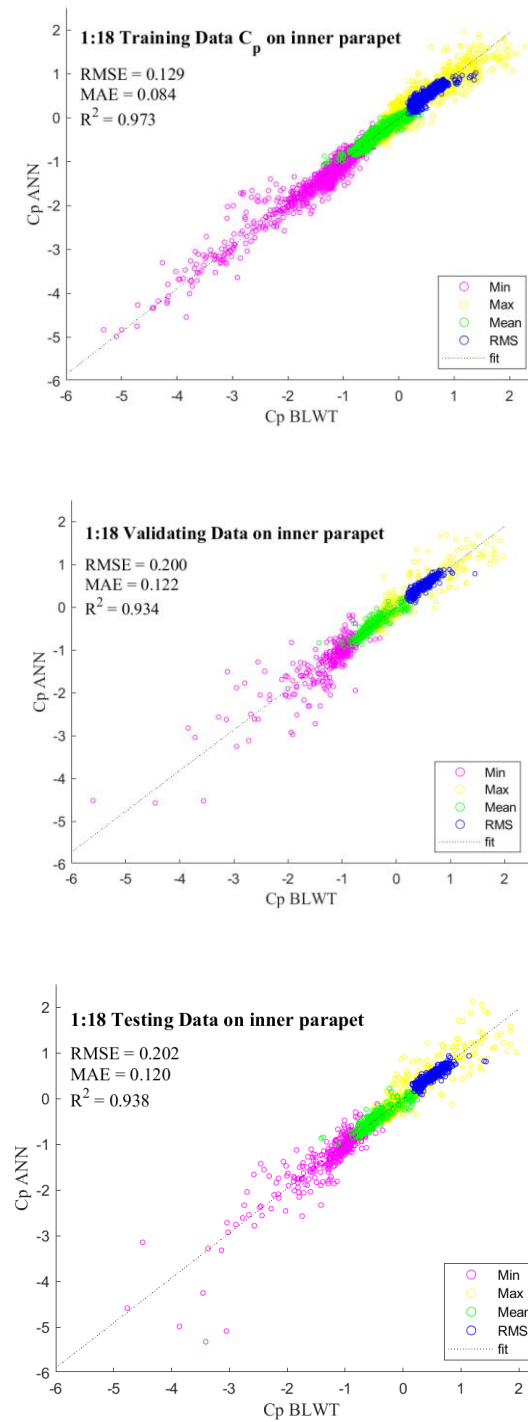


Fig 6.1.2 linear regression plots for training, validation and testing subsets of ANN model for parapets.

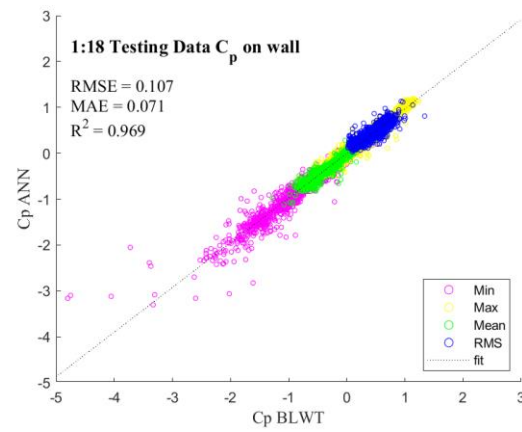
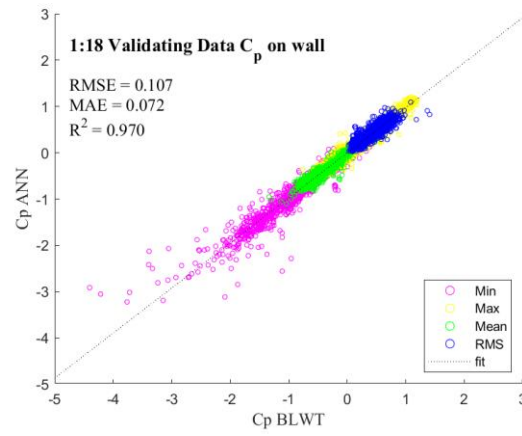
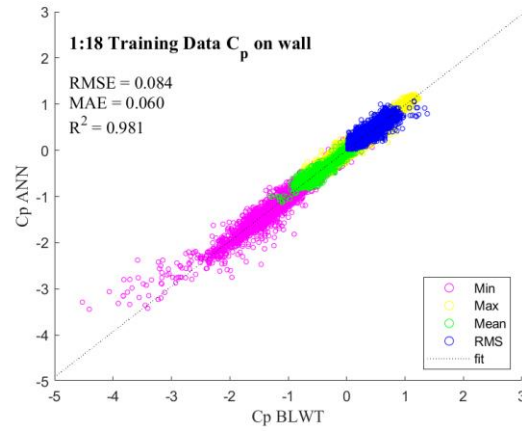


Fig 6.1.3 linear regression plots for training, validation and testing subsets of ANN model for walls.

6.1.2 Performance Evaluation by Learning Curve

Another way to evaluate the generalization performance of the trained model is through observation of learning curves which reports the MSE at the best epoch. For each ANN model, learning curves were generated by the MATLAB toolbox which shows the mean squared error of training, validation, and testing at each epoch. From Fig 6.1.4 to 6.1.6, it's observed that MSE decreases gradually at each training epoch, and three curves eventually land on a small value and remain stable as epoch further increases. The curves for training always have the lowest MSE than testing and validation. The relative distance between each curve is due to the randomness of data selection and data division. The ANN model trained on roof data has the best performance among the three models because of provided large datasets for the machine to learn from it. The same rule applies to the parapet and wall ANN models which have identical network structures.

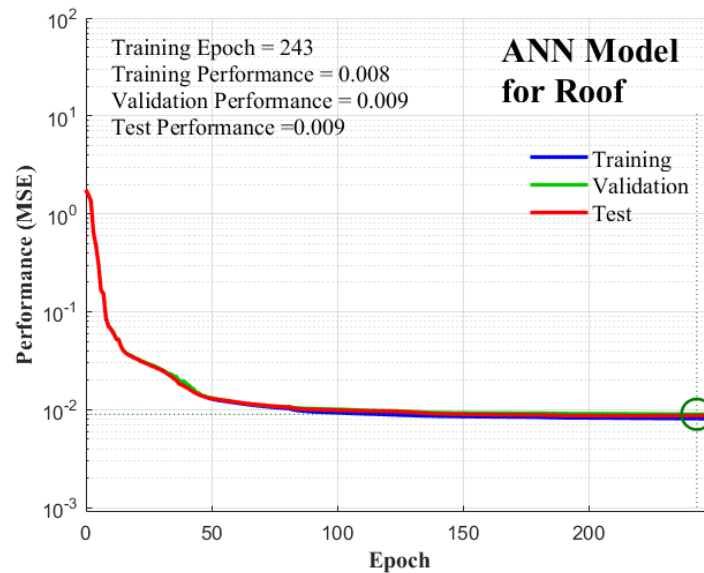


Fig 6.1.4 Learning Curves for ANN model developed with Roof data subsets.

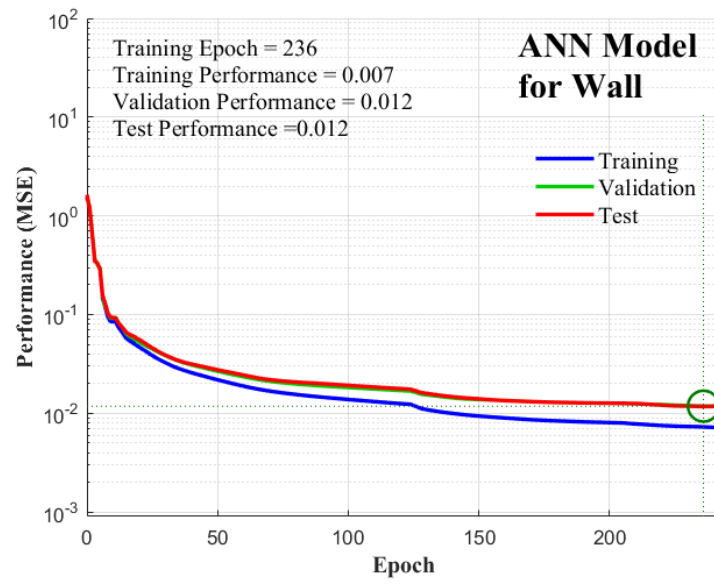


Fig 6.1.5 Learning Curves for ANN model developed with Wall data subsets.

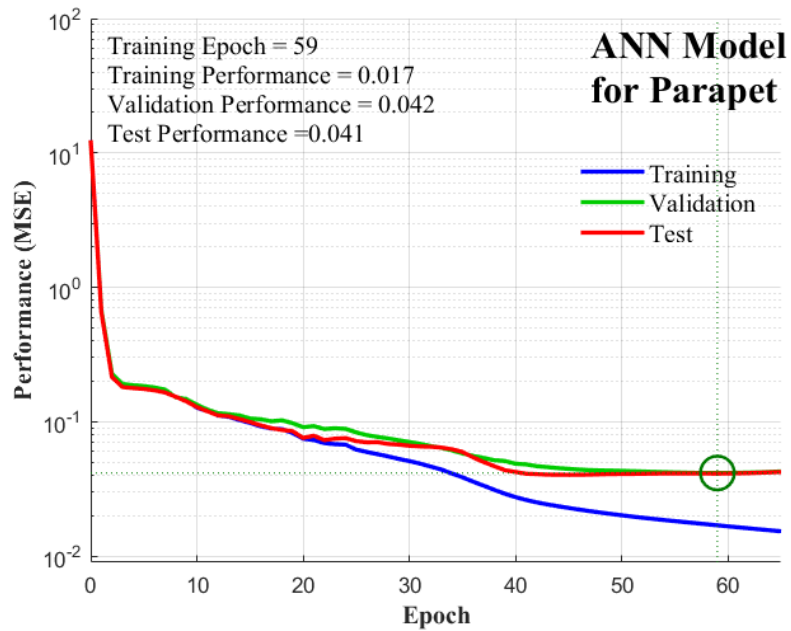


Fig 6.1.6 Learning Curves for ANN model developed with Parapet data subsets.

6.1.3 Performance Evaluation by Pressure Distribution

The generalization ability of the three networks were validated and presented in previous section by linear regression plots and learning curves. It's shown that developed ANN models were able to capture the underlying target function and populate the C_p values on the surfaces of the building model. To visibly evaluate the prediction performance of ANN models, the populated C_p was plotted on the surfaces to form pressure contour plots. The Fig 6.1.7 to 6.1.12 shows the contour map of $C_{p,Min}$ from the experiment result and ANN result side by side. The Fig 6.1.13 to 6.1.18 shows the contour map of $C_{p,Max}$ from the experiment result and ANN result. The majority of these two maps are identical by following the same trend of wind effect on certain surfaces. From time to time, there're a couple of roof taps that have slightly higher $C_{p,Min}$ than that of the contour plot from the experiment result.

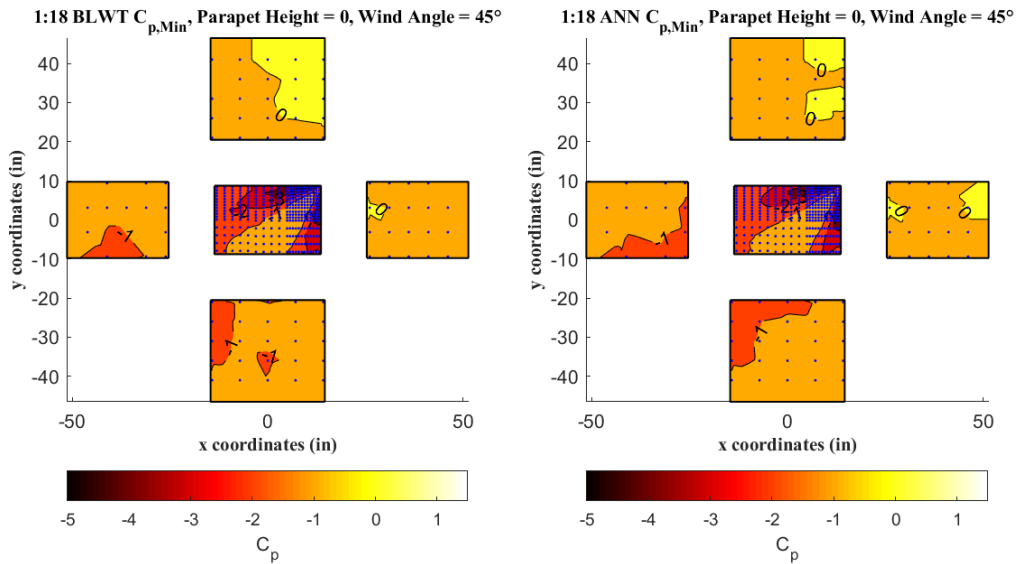


Fig 6.1.7 Pressure distribution contour of $C_{p,Min}$ from experiment result (Left) and ANN prediction (Right) at 0'' parapet and 45° wind angle.

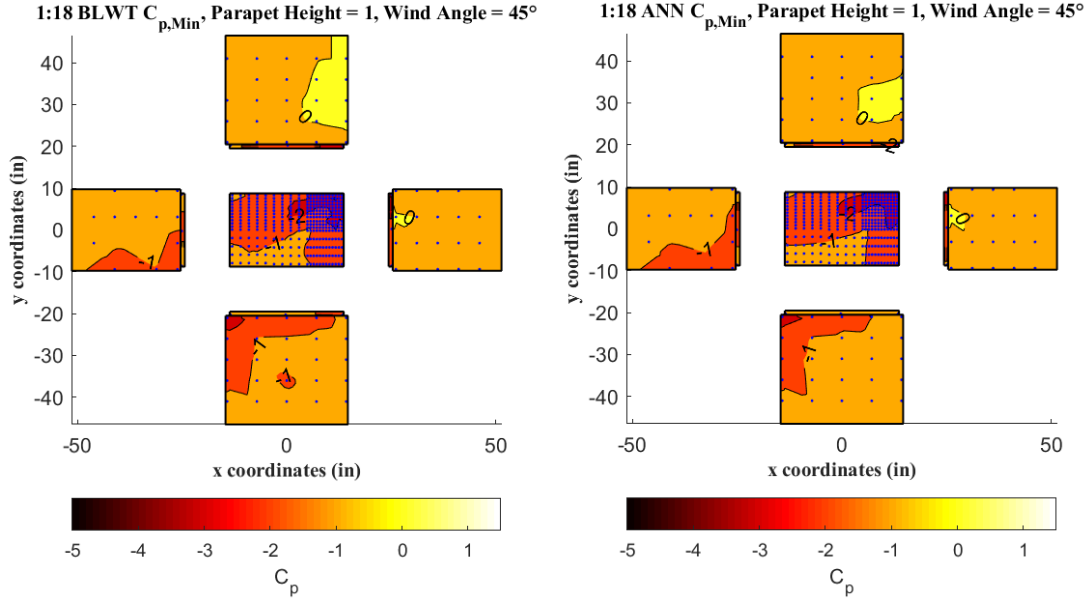


Fig 6.1.8 Pressure distribution contour of $C_{p,Min}$ from experiment result (Left) and ANN prediction (Right) at 1'' parapet and 45° wind angle.

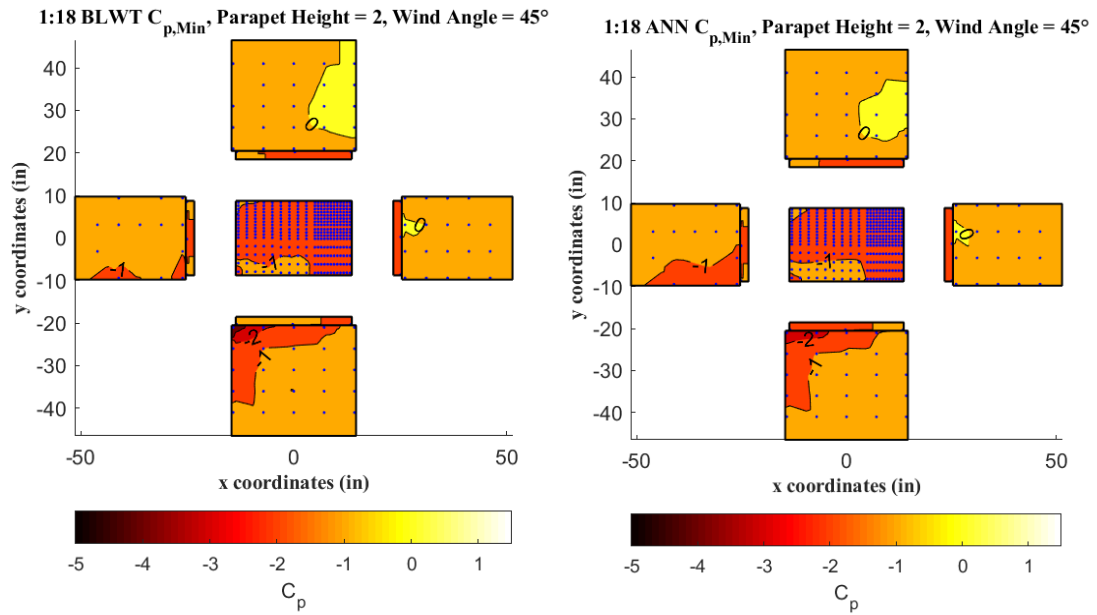


Fig 6.1.9 Pressure distribution contour of $C_{p,Min}$ from experiment result (Left) and ANN prediction (Right) at 2'' parapet and 45° wind angle.

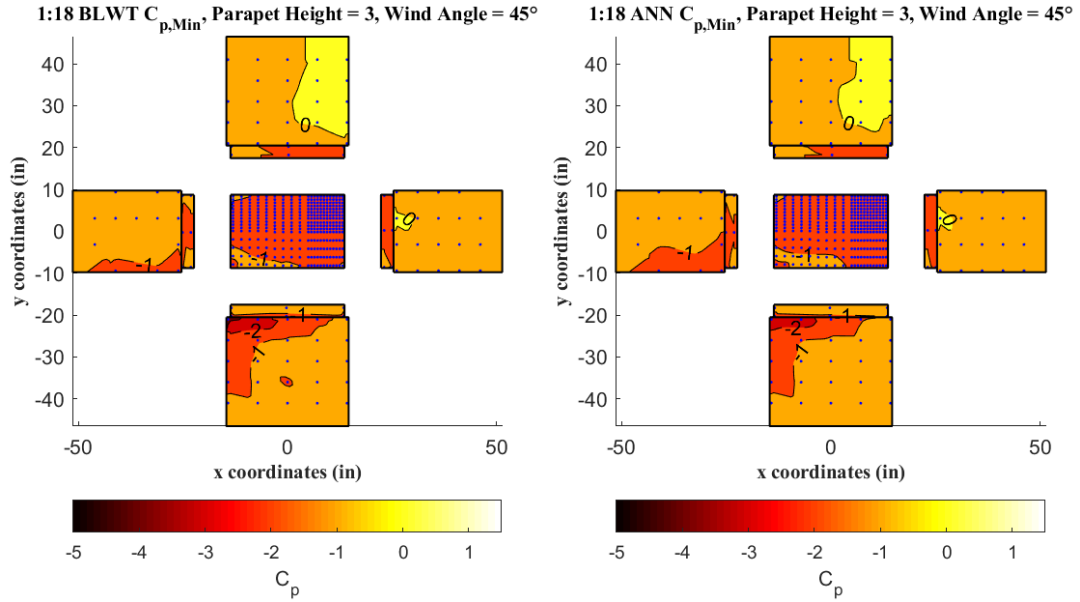


Fig 6.1.10 Pressure distribution contour of $C_{p,Min}$ from experiment result (Left) and ANN prediction (Right) at 3'' parapet and 45° wind angle.

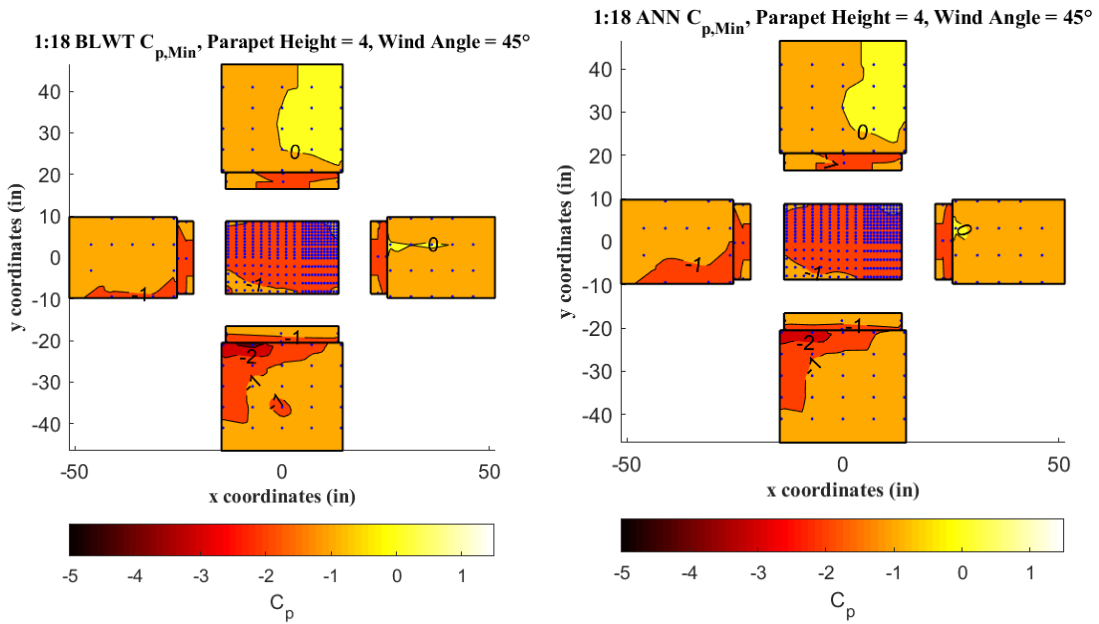


Fig 6.1.11 Pressure distribution contour of $C_{p,Min}$ from experiment result (Left) and ANN prediction (Right) at 4'' parapet and 45° wind angle.

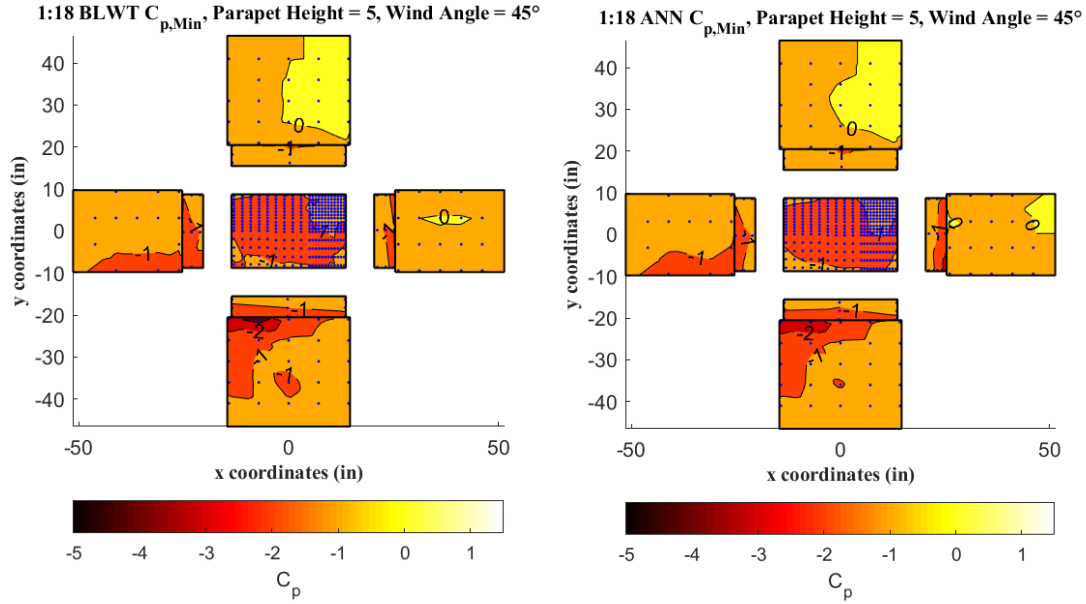


Fig 6.1.12 Pressure distribution contour of $C_{p,Min}$ from experiment result (Left) and ANN prediction (Right) at 5'' parapet and 45° wind angle.

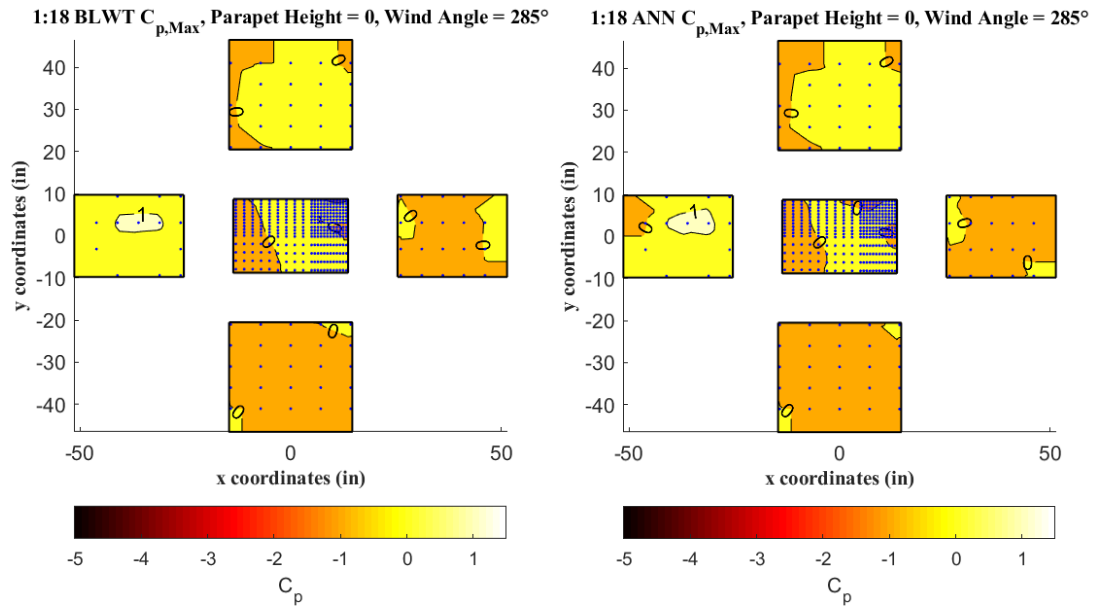


Fig 6.1.13 Pressure distribution contour of $C_{p,Max}$ from experiment result (Left) and ANN prediction (Right) at 0'' parapet and 285° wind angle.

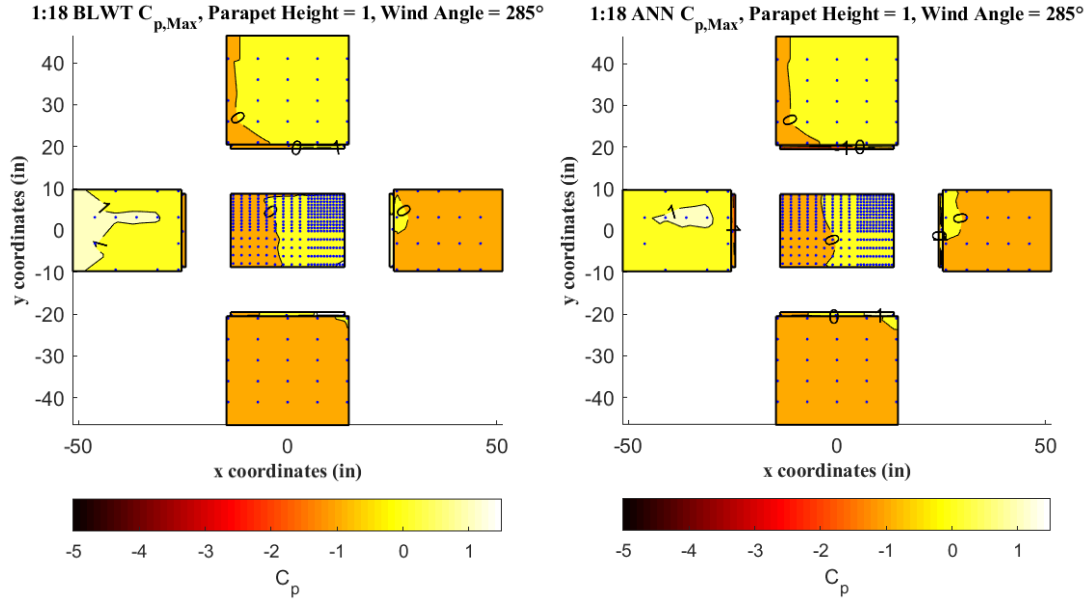


Fig 6.1.14 Pressure distribution contour of $C_{p,Max}$ from experiment result (Left) and ANN prediction (Right) at 1'' parapet and 285° wind angle.

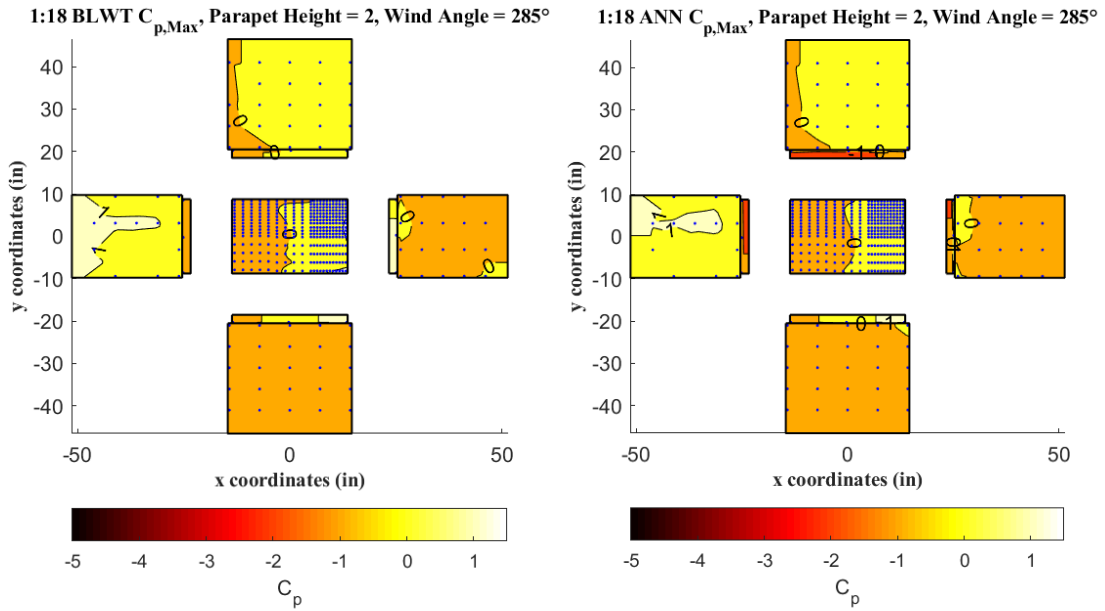


Fig 6.1.15 Pressure distribution contour of $C_{p,Max}$ from experiment result (Left) and ANN prediction (Right) at 2'' parapet and 285° wind angle.

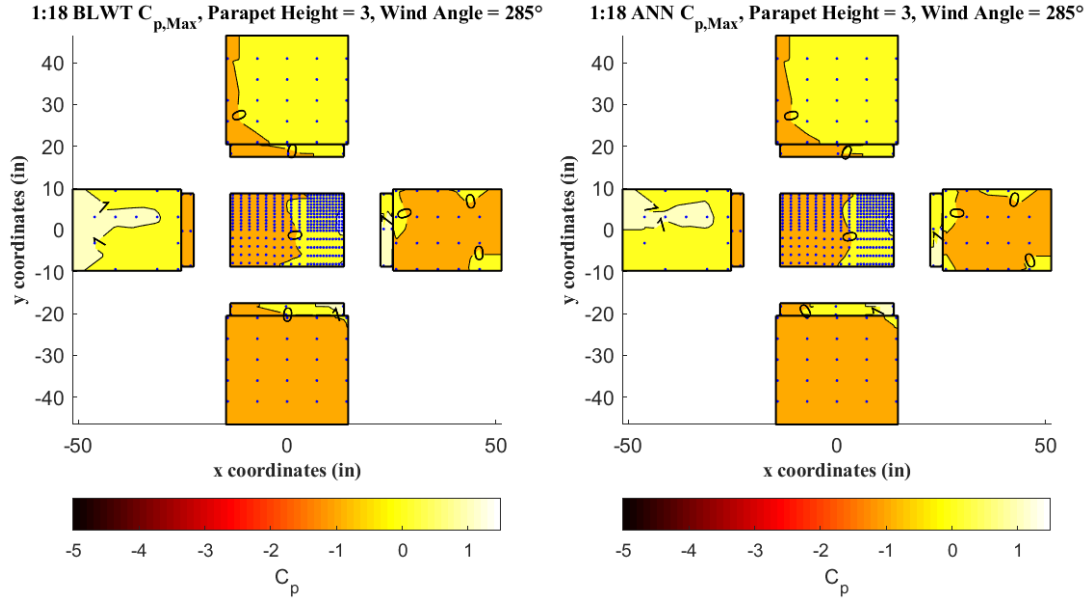


Fig 6.1.16 Pressure distribution contour of $C_{p,Max}$ from experiment result (Left) and ANN prediction (Right) at 3'' parapet and 285° wind angle.

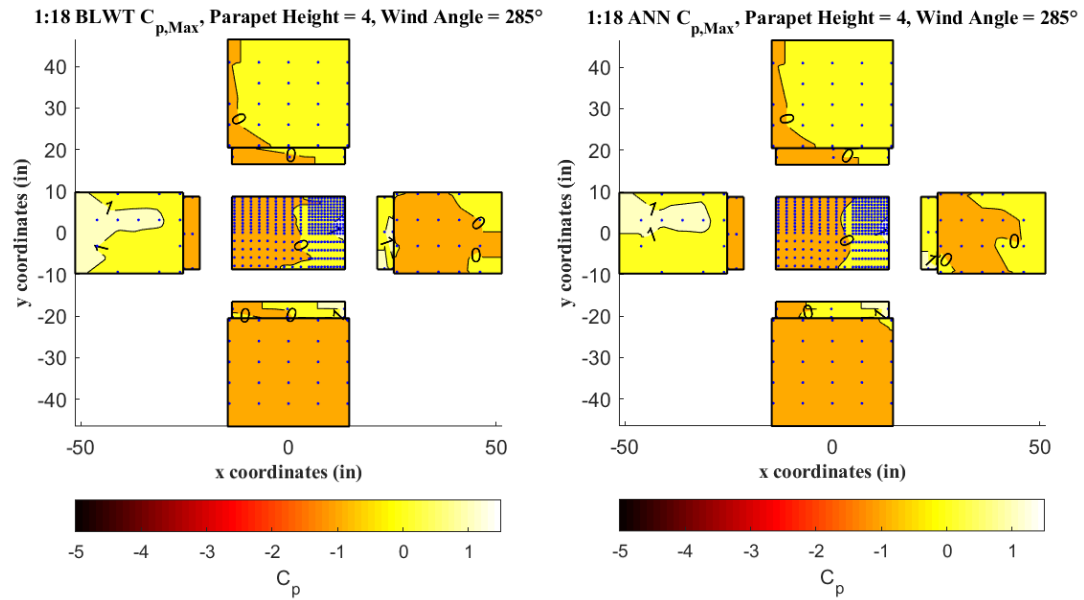


Fig 6.1.17 Pressure distribution contour of $C_{p,Max}$ from experiment result (Left) and ANN prediction (Right) at 4'' parapet and 285° wind angle.

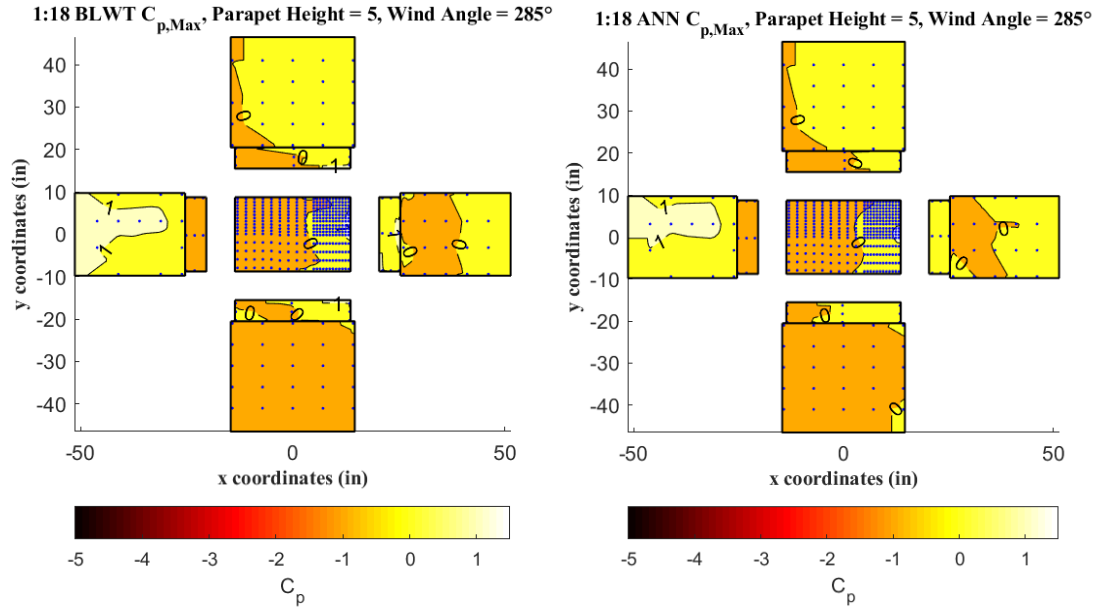


Fig 6.1.18 Pressure distribution contour of $C_{p,Max}$ from experiment result (Left) and ANN prediction (Right) at 5" parapet and 285° wind angle.

6.2 Application of ANN Model

Now that the generalization ability of ANN models was validated, the models were used to extrapolate values and unveil the relationship between parapet height and C_p . For each parapet height from 0" to 5" at every 0.5" increment, the $C_{p,Min}$ and $C_{p,Max}$ were found on the rooftop from the predicted results that contain values for 24 wind angles. In Fig 6.2.1, the scatter plot was created by plotting the Minima of $C_{p,Min}$ along the horizontal axis and the Maxima of $C_{p,Max}$ along the vertical axis.

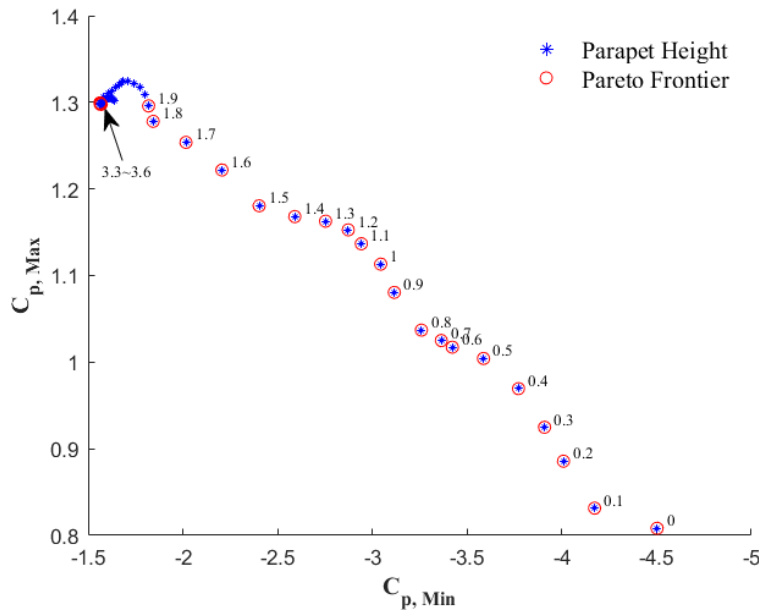


Fig 6.2.1 Relationship between $C_{p,Min}$ and $C_{p,Max}$ at Various Parapet Height

The horizontal axis was inverted for the right-hand side to represent the worst condition. As discussed previously, change in parapet height has the opposite effect on the negative and positive pressure on the rooftop. In the case of multi-objective optimization, all options that result in the most favorable condition between two criteria are Pareto efficient. The objective of minimizing the negative effect was accomplished by determining the Pareto frontier that's formed by connecting all

Pareto efficient points. There's no single optimized height in the current problem settings. Based on the preference and objective of a designer, there're generally three options which are either to provide stiffer uplift-resisting member or stronger member to resist gravity load or go with any of the intermediate options. Shown by the trend in Fig 6.2.1, moving from the bottom right corner to the upper left corner, the magnitude of $C_{p,Min}$ decrease as magnitude of $C_{p,Max}$ increase. As parapet height increase from 0" to 1.9", the tradeoff between the $C_{p,Min}$ and the $C_{p,Max}$ can be observed, and the mitigation effect grows rapidly at the corner and edges. As parapet continues to increase from 1.9", the parapet's effect grows mildly and the magnitude of both $C_{p,Min}$ and $C_{p,Max}$ fluctuates within a small range. At parapet height range of 3.3" to 3.6", the magnitude of $C_{p,Min}$ reaches the global lowest value. As parapet continuous to increase, the magnitude of $C_{p,Min}$ started to increase which's against the will of mitigate peak suction.

Based on the observed result, two conclusions were made regarding parapet's effect to the pressure coefficients on the rooftop.

1. Relative parapet height between 0.16h to 0.18h works best for roof components sensitive to uplift forces. (i.e. shingles, etc.)
2. Relative parapet height of 0~0.1h would interfere less with gravity load

6.3 Chapter Summary

In this chapter, ANN models were validated and tested by corresponding data subsets. The learning curves and linear regression plots were used to present the generalization performance of developed models. From the perspective of wind engineering, the pressure distributions were presented by a series of contour maps which shows the predicted $C_{p,Min}$ on building surface panels. The contour maps were compared to those from experimental results. After validated the performance of ANN models, the models were used to extrapolate $C_{p,Min}$ and $C_{p,Max}$ at building models with unseen parapet height. Based on the observed relationship between $C_{p,Min}$ and $C_{p,Max}$, a range of optimized heights were found to be effective at balancing negative and positive pressure on different regions of the rooftop.

Chapter 7: Conclusions and Recommendations

7.1 Conclusions

The thesis is mainly comprised of two parts, one of which focused on developing and validate the experimental database obtained from series of BLWT tests, and the other part focused on developing the accurate computational model to extend the wind pressure database. With BLWT experimental results, the thesis first investigated the wind loads on surfaces of the low-rise building protected by a solid perimetric parapet. At cornering wind angle, the $C_{p,Min}$ on the rooftop was determined at various parapet height. By observing the transition of the high suction region, the mitigation effect of the parapet was demonstrated through the pattern of pressure distribution on contour maps. The experimental result was further validated by comparing it with ASCE7-16. The experimental result of the pressure coefficient on building panels is mostly agreed with that from the ASCE7-16.

In the second part of the thesis, the objective of using the computational model to expand aerodynamic databases to a larger variety of geometries was accomplished, and the practical feasibility was approved by extending the database with previously unseen parapet height. Based on the error measure from linear regression, the performance of the roof and wall model were proved to be excellent at predicting the Mean, RMS, Min and Max of pressure coefficients. There's a relatively large error regarding the $C_{p,Min}$ and $C_{p,Max}$ of the parapet model. The parapet model has a mean averaged error of 17.7% regarding $C_{p,Max}$ and a mean averaged error of 16.8% regarding $C_{p,Min}$.

With the well-developed ANN models, the $C_{p,Min}$ and $C_{p,Max}$ were predicted for intermediate parapet height from 0 to 5” at every 0.1” of increment. The Pareto frontier was developed to demonstrate all possible optimization options to adjust the tradeoff between positive and negative wind pressure. For roof C&C like flashing and shingles, that are sensitive to roof suction load, a relative parapet height of 0.16H to 0.18H would help to mitigate the peak suction. For any structures sitting on the roof surface that mostly bears gravity load, a relative parapet height of 0 to 0.1H would interfere less with the structure’ gravity load design.

7.2 Future Studies

1. Discover all related input parameters to improve generalization performance.
2. Discover the potential of combining 3 different neural network models into one general model.
3. Consider incorporating the top of the parapet into the study to completely capture the response of parapet to wind loads.
4. Collect more experimental data for better accuracy at walls and parapets.

Bibliography

Abu-Mostafa, Y. S., Magdon-Ismail, M., & Lin, H.-T. (2012). Learning from data: a short course. Estados Unidos: AMLBook.

Anderson, J. D. (2011). *Fundamentals of aerodynamics*. London: Mcgraw-hill Publishing Co.

ASCE 7-16 (2016). Minimum Design Loads for Buildings and Other Structures, American Society of Civil Engineers, Reston, VA.

Barlow, H. B. (1989). Unsupervised Learning. *Neural Computation*, 1(3), 395–311.

Bre, F., Gimenez, J. M., & Fachinotti, V. D. (2018). Prediction of wind pressure coefficients on building surfaces using artificial neural networks. *Energy and Buildings*, 158, 1429–1441. doi: 10.1016/j.enbuild.2017.11.045

Chen, Y., Kopp, G., & Surry, D. (2003). Prediction of pressure coefficients on roofs of low buildings using artificial neural networks. *Journal of Wind Engineering and Industrial Aerodynamics*, 91(3), 423–441. doi: 10.1016/s0167-6105(02)00381-1

Dreyfus, S. (1962). The numerical solution of variational problems. *Journal of Mathematical Analysis and Applications*, 30–45.

Emes, Matthew & Jafari, Azadeh & Arjomandi, Maziar. (2018). Estimating the Turbulence Length Scales from Cross-Correlation Measurements in the Atmospheric Surface Layer.

Fang, C., & Sill, B. L. (1995). Pressure distribution on a low-rise building model subjected to a family of boundary layers. *Journal of Wind Engineering and Industrial Aerodynamics*, 56(1), 87–105. doi: 10.1016/0167-6105(94)00008-2

Fernández-Cabán PL, Masters FJ and Phillips BM (2018) Predicting Roof Pressures on a Low-Rise Structure From Freestream Turbulence Using Artificial Neural Networks. *Front. Built Environ*. 4:68. doi: 10.3389/fbuil.2018.00068

Holmes, J. D. (2017). *Wind loading of structures*. Boca Raton, FL: CRC Press.

Huang, P., Peng, X., & Gu, M. (2017). Wind tunnel study on effects of various parapets on wind load of a flat-roofed low-rise building. *Advances in Structural Engineering*, 20(12), 1907–1919. doi.org/10.1177/1369433217700425

Kopp, G. A., Surry, D., & Mans, C. (2005^a). Wind effects of parapets on low buildings: Part 1. Basic aerodynamics and local loads. *Journal of Wind Engineering and Industrial Aerodynamics*, 93(11), 817–841. doi: 10.1016/j.jweia.2005.08.006

- Kopp, G. A., Mans, C., & Surry, D. (2005^b). Wind effects of parapets on low buildings: Part 2. Structural loads. *Journal of Wind Engineering and Industrial Aerodynamics*, 93(11), 843–855. doi: 10.1016/j.jweia.2005.08.005
- Kopp, G. A., Morrison, J. M. (2018). Component and Cladding Wind Loads for Low-Slope Roofs on Low-Rise Buildings. *Journal of Wind Engineering and Industrial Aerodynamics*. doi.org/10.1061/(ASCE)ST.1943-541X.0001989
- Lythe, R. G. & Surry, D. (1983) 'Wind Loading of Flat Roofs with and without Parapets' *Journal of Wind Engineering and Industrial Aerodynamics*, 11, pp. 75-94
- Pan, X., Lee, B., Zhang, C. (2013). A comparison of neural network backpropagation algorithms for electricity load forecasting. *Intelligent Energy Systems (IWIES)*, IEEE International Workshop on, vol., no., pp.22,27, 14-14.
- Peterka, J. A., (1989) 'Roof Uplift Mechanisms' *Proceedings of the Roof Wind Uplift Testing Workshop*, pp. 61-66.
- Phillips, Brian; Masters, Forrest (2019). Cyber-Physical Systems Approach for the Optimal Design in Wind Engineering: Parapet Walls. *DesignSafe-CI*. <https://doi.org/10.17603/ds2-p8wj-ey61>
- Schmidhuber, J. (2015). Deep learning in neural networks: An overview. *Neural Networks*, 61, 85–117. doi: 10.1016/j.neunet.2014.09.003
- Sisi Ma (2020). find_pareto_frontier. MATLAB Central File Exchange. Retrieved from: https://www.mathworks.com/matlabcentral/fileexchange/45885-find_pareto_frontier
- Stathopoulos, T. (1982). Wind loads on low-rise buildings: a review of the state of the art. *Engineering Structures* 6: 119–35.
- Suaris, W., & Irwin, P. (2010). Effect of roof-edge parapets on mitigating extreme roof suctions. *Journal of Wind Engineering and Industrial Aerodynamics*, 98(10-11), 483–491. doi: 10.1016/j.jweia.2010.03.001
- Whiteman, M. L., Phillips, B. M., Fernández-Cabán, P. L., Masters, F. J., Bridge, J. A., & Davis, J. R. (2018). Optimal design of structures using cyber-physical wind tunnel experiments with mechatronic models. *Journal of Wind Engineering and Industrial Aerodynamics*, 172, 441–452. doi: 10.1016/j.jweia.2017.11.013